Thermal impact on the excavation damage zone around a supported drift using the 2^{nd} gradient model

Hangbiao Song[1*], Gilles Corman[1] and Frédéric Collin[1]

[1*]Urban and Environmental Engineering Research Unit, Université de Liège, Allée de la Découverte 9, 4000, Liège, Belgium.

*Corresponding author(s). E-mail(s): hangbiao.song@uliege.be;

Abstract

The temperature increase induced by radioactive waste decay generates the thermal pressurisation around the excavation damage zone (EDZ), and the excess pore pressure could induce fracture re-opening and propagation. Shear strain localisation in band mode leading to the onset of micro/macro cracks can be always evidenced before the fracturing process from the lab experiments using advanced experimental devices, hence the thermal effects on the rock behaviour around the EDZ could be modelled with the consideration of development of shear bands. A coupled local $\mathbf{2^{nd}}$ gradient model with regularisation technique is implemented, considering the thermo-hydro-mechanical (THM) couplings in order to well reproduce the shear bands. Furthermore, the thermo-poro-elasticity framework is summarized to validate the implemented model. The discrepancy of thermal dilation coefficient between solid and fluid phases is proved to be the significant parameter leading to the excess pore pressure. Finally, an application of a heating test based on Eurad Hitec benchmark exercise with a drift supported by a liner is studied. The strain localisation induced by thermal effects is properly reproduced. The plasticity and shear bands evolutions are highlighted during the heating, and the shear bands are preferential to develop in the minor horizontal principal stress direction. Different shear band patterns are obtained with changing gap values between the drift wall and the liner. A smaller gap between the wall and the liner can limit the development of shear bands.

Keywords: Numerical modelling, Thermal effects, THM couplings, strain localisation, shear bands

1 Introduction

The deep geological disposal is recognised as one of the most reliable solution for long-term management of radioactive waste. Specifically, the waste within the canisters is stored into low permeable formations, to build a natural barrier between waste and biosphere (Félix et al., 1996; Neerdael and Boyazis, 1997; Croisé et al., 2004). In addition, radioactive waste decay also generates a certain amount of heat leading to elevated temperature (over 70°C and sometimes over 100°C) (Collin et al., 2002). To take all the physical processes into account, the characterisation of the *in-situ* THM behaviour of the clay host rock is mandatory for the design of the underground radioactive waste disposal facilities and to provide long-term safety.

Indeed, the heat generated by the waste must not affect the favourable properties of the clay host rock for containment, especially its transport properties (Bossart et al., 2002). However, the temperature increase evidenced around the repository may affect the THM behaviour of formations. In the near-field (the vicinity of drift), due to the discrepancy of thermal expansion coefficient between solid and fluid phases, the excess pore pressure generated by the thermal dilation of pore water could induce fracture re-opening or propagation (Wileveau et al., 2007; Gens et al., 2011). In the far-field, due to symmetric conditions, the half-way zone between two neighbouring cells will be subjected to thermal loading from both sides. Depending on the distance between the cells and the intensity of the thermal load, this could induce tensile or even shear failure (Plúa et al., 2021; Braun et al., 2022). The above behaviour may potentially alter the permeability of host rock as a result. To investigate the thermal effects on the THM behaviour of the host rock, some underground research laboratories (URL) have been already developing large scale *in-situ* heating tests, for instance in the HADES URF in Belgium (CERBERUS, ATLAS and PRACLAY tests) (De Bruyn and Labat, 2002; Dizier et al., 2021), in the Mont Terri URL in Switzerland (HE-D test) (Jobmann and Polster, 2007; Garitte et al., 2017), and in the Meuse/Haute-Marne URL in France (TED, EPT, ALC1604, ALC1605 and CRQ tests) (Conil et al., 2020; Seyedi et al., 2021; Bumbieler et al., 2021; Armand et al., 2017; Narkuniene et al., 2022).

The thermal pressurisation occurs both in the near field where the fractures exist in EDZ and in the far field where the host rock is intact before heating. An appropriate constitutive law including thermal effect should be defined to highlight the THM coupling of the host formation. The earliest simulation to introduce the conformity between mechanical theory and thermodynamics can be dated back to last century (Dirksen, 1970). The strain variation induced by thermal effects displays a strong dependency on the overconsolidation ratio of clay, leading to reversible dilation or irreversible compression. Hueckel and Borsetto (1990) firstly came up with a constitutive law including thermal plasticity for saturated soils. The strain compensation between thermal softening and plastic hardening was revealed as a result of thermal

consolidation. Modaressi and Laloui (1997) extended the simulation to thermo-viscoplastic behaviour under cyclic loading, where the thermal hardening and the dependency of yield surface on temperature were considered. An isotropic thermo-mechanical path was presented by Laloui and Cekerevac (2003), where the effect of preconsolidation pressure and induced thermal strain on the void ratio change was highlighted. There is also some research work showing that soil characteristics like friction angle, elastic modulus and water viscosity are influenced by the rise of temperature (Laloui, 2001). The above models were implemented especially for fine-grained porous materials which are poorly consolidated, and the strong dependency on the preconsolidation pressure was shown in such kind of soils. For overconsolidated geomaterials like claystone, most of the studies conclude that the volume increase under thermal loading is more pronounced due to the expansion of mineral particles and adsorbed water, while thermal contraction decreases with increases in overconsolidation ratio (Cui et al., 2000; Romero et al., 2005). The *in-situ* stress level of claystone is lower than its preconsolidation pressure, then an internal frictional model combined with thermoelasticity is usually used (Chen et al., 2021; Tourchi et al., 2021). The yield surfaces for friction model are described by Mohr-Coulomb criterion, where the linearity is valid both in the Coulomb plane and the (p,q) plane. In order to solve the discontinuous derivable problem numerically, approximations of Mohr-Coulomb criterion are used, namely the Drucker Pragaer criterion and the Van Eekelen criterion among others. The isotropic hardening and softening of yield surface are available in the frictional model.

The *in-situ* THM behaviour of the clay rock in the near field is particularly investigated in this study, thus the crucial issue is to well understand and predict the behaviour of the rock in the excavation damage zone (EDZ) (Bossart et al., 2004; Tsang et al., 2005), which is mostly dominated by irreversible property changes of rock, such as permeability increase. The *in-situ* and laboratory experiments show the damage type of clay rock can be considered as crack initiation and propagation, and the strain localisation in shear band mode can characterise the damage as an indicator of fracturing process (Diederichs, 2003). However, classical finite element methods suffer the mesh-dependency problem, both of mesh size and orientation, as illustrated by Pietruszczak and Mroz (1981), Zervos et al. (2001a), Collin et al. (2009), and Wu and Wang (2010). This dependency problem can be addressed by employing an appropriate regularisation method. On the one hand, such method introduces an internal length scale by developing non-local approaches (Pijaudier-Cabot and Bažant, 1987; Peerlings et al., 1996). On the other hand, the enrichment of microstructure kinematics is taken into account (Germain, 1973). Among a large amount of enhanced models, the coupled local second gradient model developed in 3SR laboratory (University Grenoble-Alpes) is particularly used in this study, which is able to well reproduce the development of strain localisation (Chambon et al., 1998, 2001). This model was initially proposed to implement continuum with microstructure effect in local framework. Collin et al. (2006) further developed the model from monophasic

to biphasic porous medium. This model was extended to multiphasic porous media under unsaturated conditions by Pardoen et al. (2015a). A good agreement was obtained between the numerical solutions with implemented model and *in-situ* observations around the EDZ (Pardoen et al., 2016; Pardoen and Collin, 2017).

The next step is to further investigate the temperature effect on the THM behaviour of clay host rock. Thermal pressurisation has already been evidenced both in laboratory (Braun et al., 2022; Monfared et al., 2012) and *in-situ* heating tests (Bumbieler et al., 2021). As for modelling the strain localisation, biaxial compression tests were carried out to represent the fracturing in shear band mode, among which the microstructure effect was also taken into account (Shahrokhabadi et al., 2020; Sun, 2015; Rattez et al., 2018). Nevertheless, the reproduction of strain localisation in large-scale still needs further investigations. A 3D numerical model about the ALC1604 *in-situ* heating test was carried out by Tourchi et al. (2021), where a steel casing around the heaters and an air gap between the rock and casing are specially treated. Yu et al. (2021) reproduced the evolution of damage zones around the ALC1604 heating borehole, which shows the damage zone evolution is largely controlled by the tensile cracks rather than the shear cracks. In this paper, the thermo-mechanical constitutive model is an elastoplastic model coupled with thermoelasticity, due to strong overconsolidation state of candidate host rock (Callovo-Oxfordian claystone). The overall objective of the present work is to reproduce the temperature effect on the EDZ in the host rock using local second gradient model, to help optimize the repository design.

2 Coupled Local Second Gradient Model

According to Coussy (2004), the rock material is a porous medium made up by a continuous mixture. The solid phase composes the solid skeleton with grains assembly, while the fluid phase in porous space between solid grains includes the liquid and gaseous phases. In this study, the rock material is considered as fully saturated, hence the phase transfers like evaporation are not taken into account.

2.1 Balance equation

The balance equations are written in current deformed configuration denoted Ω^t. The momentum and energy balance are written for the whole mixture, while the mass balance is presented for the fluid phase. The governing equations of a medium with microstructure can be tracked from the work of Cosserat and Cosserat (1909) and Germain (1973). In the context of microstructure continuum theory, a microkinematic gradient field v_{ij} is introduced to describe the strain and rotation at microscale. Accordingly, additional terms corresponding to classical continuum mechanics are added in the internal

virtual work. For any virtual displacement field u^*, the internal work reads:

$$W^*_{int} = \int_{\Omega^t} \left(\sigma^t_{ij} \frac{\partial u^*_i}{\partial x^t_j} + \tau^t_{ij}(v^*_{ij} - F^*_{ij}) + \Sigma^t_{ijk} h^*_{ijk} \right) d\Omega^t \tag{1}$$

where W^*_{int} is the virtual work of internal forces and σ^t_{ij} is the Cauthy stress field. $\frac{\partial u^*_i}{\partial x^t_j} = F^*_{ij}$ is the virtual macrodeformation gradient, τ^t_{ij} is the additional stress related to microstructure, v^*_{ij} is the virtual microkinematic gradient, h^*_{ijk} is the virtual micro second gradient, and Σ^t_{ijk} is the double stress dual of h^*_{ijk}. The external virtual work can be defined as:

$$W^*_{ext} = \int_{\Omega^t} \rho^t g_i u^*_i d\Omega^t + \int_{\Gamma^t_\sigma} \left(\bar{t}^t_i u^*_i + \bar{T}^t_i v^*_{ik} n^t_k \right) d\Gamma^t \tag{2}$$

where ρ is the density of the porous mixture, g_i is the gravitational acceleration. $\bar{t}_i$ is the classical external traction force per unit area, $\bar{T}_i$ is an additional external double force per unit area, both applied on a part of Γ^t_σ of the boundary of Ω^t.

An assumption is added in the local second gradient model, in which the equality between the microkinematic and macrodeformation gradients is achieved, $v_{ij} = F_{ij}$ leading to $v^*_{ij} = F^*_{ij}$. This assumption is introduced through a field of Lagrange multipliers λ_{ij} (Chambon et al., 1998). The momentum balance equation is expressed by the equality between internal and external virtual works in a weak form:

$$\begin{aligned} &\int_{\Omega^t} \left(\sigma^t_{ij} \frac{\partial u^*_i}{\partial x^t_j} + \Sigma^t_{ijk} \frac{\partial v^*_{ij}}{\partial x^t_k} \right) d\Omega^t - \int_{\Omega^t} \lambda^t_{ij} \left(\frac{\partial u^*_i}{\partial x^t_j} - v^*_{ij} \right) d\Omega^t \\ &\quad = \int_{\Omega^t} \rho^t g_i u^*_i d\Omega^t + \int_{\Gamma^t_\sigma} \left(\bar{t}^t_i u^*_i + \bar{T}^t_i v^*_{ik} n^t_k \right) d\Gamma^t \end{aligned} \tag{3}$$

$$\int_{\Omega^t} \lambda^*_{ij} \left(\frac{\partial u^t_i}{\partial x^t_j} - v^t_{ij} \right) d\Omega^t = 0 \tag{4}$$

Collin et al. (2006) extended the second gradient theory from monophasic to multiphasic medium, within the definition of Terzaghi's total stress and hypothesis of independency between microstructure effect and pore pressure. For any kinematically virtual pore pressure field p^*_w, the fluid mass balance reads in a weak form:

$$\int_{\Omega^t} \left(\dot{M}^t_w p^*_w - f^t_{w,i} \frac{\partial p^*_w}{\partial x^t_i} \right) d\Omega^t = \int_{\Omega^t} Q^t_w p^*_w d\Omega^t - \int_{\Gamma^t_{q_w}} \bar{q}^t_w p^*_w d\Gamma^t \tag{5}$$

where $\dot{M}_w^t$ is the mass variation of fluid phase, $f_{w,i}$ is the mass flow, Q_w^t is a fluid sink term and $\Gamma_{q_w}^t$ is the part of the boundary where the input fluid mass per unit area $\bar{q}_w^t$ is prescribed.

In this study, we extended the model to thermo-hydro-mechanical coupled problem assuming likewise that the temperature has no influence at the microstructure level, and that microkinematic gradient is not generated by thermal changes. The energy balance equation is defined in a weak form for every admissible virtual temperature field T^*:

$$\int_{\Omega^t} \left(\dot{S}_T^t T^* - f_{T,i}^t \frac{\partial T^*}{\partial x_i^t} \right) d\Omega^t = \int_{\Omega^t} Q_T^t T^* d\Omega^t - \int_{\Gamma_{q_T}^t} \bar{q}_T^t T^* d\Gamma^t \tag{6}$$

where $\dot{S}_T^t$ is the enthalpy variation of the porous mixture, $f_{T,i}$ is the heat flow, Q_w^t is a heat sink term and $\Gamma_{q_T}^t$ is the part of the boundary where the input heat flux per unit area $\bar{q}_T^t$ is prescribed.

2.2 Solid and fluid phase behaviour

The physical coupling process including the solid and fluid phases behaviour needs to be reproduced in Eq. 5 and Eq. 6. In fully saturated conditions, the fluid mass inside a porous material volume Ω reads:

$$M_w = \rho_w \phi \Omega \tag{7}$$

where ϕ is the porosity, and ρ_w is the density of fluid. The time derivative of the fluid mass yields for a unit mixture volume:

$$\dot{M}_w = \rho_w \left[\left(\frac{\dot{p}_w}{\chi_w} - \alpha_w \dot{T} \right) \phi + \frac{\dot{p}_w}{K_s} (b - \phi) + b \frac{\dot{\Omega}}{\Omega} \right] \tag{8}$$

where χ_w is the fluid bulk modulus, K_s is the bulk modulus of solid skeleton, b is the Biot coefficient, and α_w is the thermal expansion coefficient of fluid which is defined as a function of temperature under atmospheric pressure. As mentioned by Kell (1975), the thermal expansion of water is deduced by the derivative of water density with respect to temperature, thus the consistent relation between temperature and water density will be applied in the implemented modelling, to trigger the identical volumetric thermal expansion of fluid (Fig. 1). Eq. 8 takes into account the compressibility of the fluid and the solid grains.

The fluid flow is obtained by using the Darcy's law:

$$f_{w,i} = -\rho_w \frac{k_{ij}}{\mu_w} \left(\frac{\partial p_w}{\partial x_j} + \rho_w g_i \right) \tag{9}$$

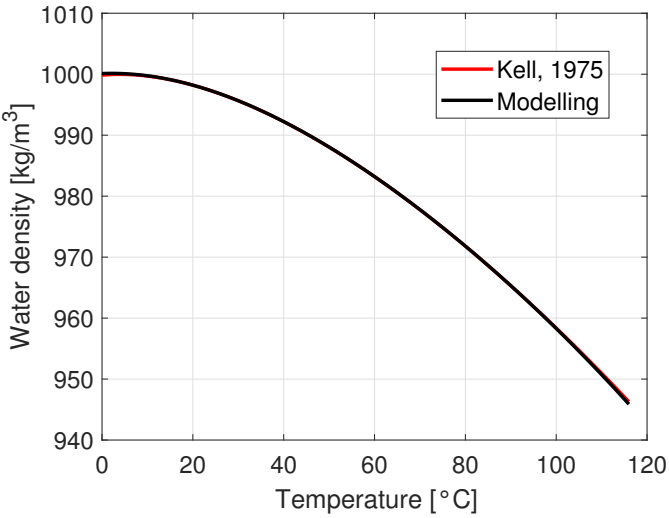

Fig. 1 Water density evolution applied in the modelling as a function of the temperature

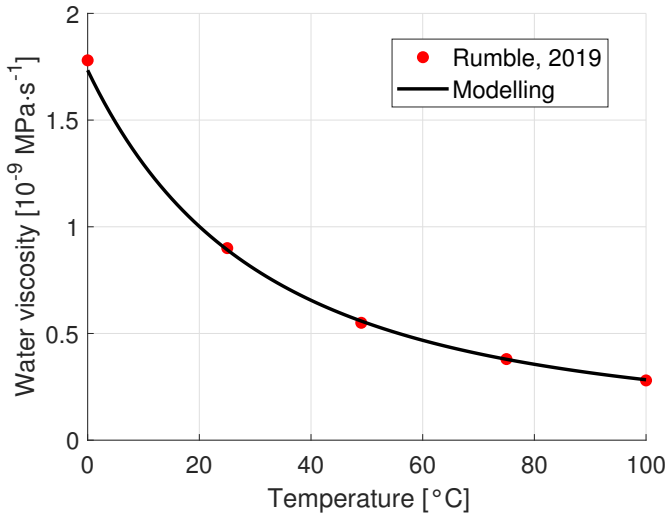

Fig. 2 Evolution of water viscosity as a function of the temperature under atmospheric pressure

where k_{ij} is the intrinsic permeability tensor and μ_w is the fluid viscosity. The evolution of water viscosity is introduced as a function of temperature under atmospheric pressure in Fig. 2 (Rumble, 2019).

The thermal model is required to reproduce heat transfer in fully saturated porous media. The enthalpy of the system is written by the sum of the enthalpy

of each component:

$$S_T = \left[\phi\rho_w c_{p,w} + (1-\phi)\rho_s c_{p,s}\right](T - T_0)\Omega \tag{10}$$

where $c_{p,w}$ and $c_{p,s}$ are the specific heat of the fluid and solid phases respectively, T_0 is the initial temperature in the reference configuration. The time derivative of the enthalpy storage reads for a unit porous volume:

$$\begin{aligned}\dot{S}_T = {} & c_{p,w}\rho_w(b-\phi)\left(\frac{\dot{\Omega}}{\Omega} + \frac{\dot{p}_w}{K_s} - \alpha_d\dot{T}\right)(T-T_0) + c_{p,w}\rho_w\phi\left(\frac{\dot{p}_w}{\chi_w} - \alpha_w\dot{T}\right)(T-T_0) \\ & + c_{p,w}\rho_w\phi\dot{T} + c_{p,w}\rho_w\phi(T-T_0)\frac{\dot{\Omega}}{\Omega} - c_{p,s}\rho_s(b-\phi)\left(\frac{\dot{\Omega}}{\Omega} + \frac{\dot{p}_w}{K_s} - \alpha_d\dot{T}\right)(T-T_0) \\ & + c_{p,s}\rho_s\left[\frac{b-\phi}{K_s}\dot{p}_w - (b-\phi)\alpha_d\dot{T} - (1-b)\frac{\dot{\Omega}}{\Omega}\right](T-T_0) \\ & + c_{p,s}\rho_s(1-\phi)\dot{T} + c_{p,s}\rho_s(1-\phi)(T-T_0)\frac{\dot{\Omega}}{\Omega}\end{aligned} \tag{11}$$

where α_d is the drained volumetric thermal expansion coefficient of the porous medium. The heat transport in saturated condition corresponds to two effects: conduction and convection by the fluid phase as expressed by the following equations:

$$f_{T,i} = -\Gamma\nabla T + c_{p,w} f_{w,i}(T - T_0) \tag{12}$$

where Γ is the mixture conductivity, it depends on the thermal properties of each component and reads:

$$\Gamma = \lambda_s(1-\phi) + \lambda_w\phi \tag{13}$$

where λ_s and λ_w are the thermal conductivities of solid and fluid phases respectively.

It is worthwhile to mention that the model used in this study takes the large strains and large rotation effects into account, thanks to the updated Lagrange method (Charlier, 1987). The equilibrium and fluid flow are both written in the actualised current configuration, hence the convection of solid phase is implicitly considered.

2.3 Coupled finite element formulation

In order to solve the previous balance equations numerically, it is imperative to discretise in time steps Δt, leading to two configurations. Provided that the configuration Ω^t at time t is in equilibrium with the boundary conditions, the aim is to determine the other Ω^τ at a time $\tau = t + \Delta t$. A guess of solution denoted as Ω^{τ_1} is out of equilibrium, thus both configurations at time t and τ_1 are assumed to be known, and the out of balance forces are defined as $\Delta_1^{\tau_1}$, $\Delta_2^{\tau_1}$, $\Delta_3^{\tau_1}$ and $\Delta_4^{\tau_1}$. The next objective is to detect a new configuration τ_2, close to τ_1,

where the out of balance forces vanish. In order to solve the problem linearly, rewriting the field equations for Ω^{τ_2} in Ω^{τ_1}, subtracting the balance equations of the two configurations, assuming that g_i, t_i, $\bar{q}_w$, $\bar{Q}_w$, $\bar{q}_T$ and $\bar{Q}_T$ are position independent and that double forces $\bar{T}_i$ vanish, a full Newton-Raphson iterative procedure is followed:

$$\begin{aligned}
&\int_{\Omega^{\tau_1}} \frac{\partial u_i^*}{\partial x_l^{\tau_1}} \left(\sigma_{ij}^{\tau_2} \frac{\partial x_l^{\tau_1}}{\partial x_j^{\tau_2}} det(F) - \sigma_{il}^{\tau_1} \right) + \frac{\partial v_{ij}^*}{\partial x_l^{\tau_1}} \left(\Sigma_{ijk}^{\tau_2} \frac{\partial x_l^{\tau_1}}{\partial x_k^{\tau_2}} det(F) - \Sigma_{ijl}^{\tau_1} \right) d\Omega^{\tau_1} \\
&- \int_{\Omega^{\tau_1}} \frac{\partial u_i^*}{\partial x_l^{\tau_1}} \left(\lambda_{ij}^{\tau_2} \frac{\partial x_l^{\tau_1}}{\partial x_j^{\tau_2}} det(F) - \lambda_{il}^{\tau_1} \right) - v_{ij}^* \left(\lambda_{ij}^{\tau_2} det(F) - \lambda_{ij}^{\tau_1} \right) d\Omega^{\tau_1} \\
&- \int_{\Omega^{\tau_1}} u_i^* \left(\rho^{\tau_2} det(F) - \rho^{\tau_1} \right) g_i d\Omega^{\tau_1} = -\Delta_1^{\tau_1}
\end{aligned} \tag{14}$$

$$\int_{\Omega^{\tau_1}} \lambda_{ij}^* \left(\left(\frac{\partial u_i^{\tau_2}}{\partial x_k^{\tau_1}} \frac{\partial x_k^{\tau_1}}{\partial x_j^{\tau_2}} det(F) - \frac{\partial u_i^{\tau_1}}{\partial x_j^{\tau_1}} \right) - \left(v_{ij}^{\tau_2} det(F) - v_{ij}^{\tau_1} \right) \right) d\Omega^{\tau_1} = -\Delta_2^{\tau_1} \tag{15}$$

$$\int_{\Omega^{\tau_1}} p_w^* \left(\dot{M}_w^{\tau_2} det(F) - \dot{M}_w^{\tau_1} \right) - \frac{\partial p_w^*}{\partial x_l^{\tau_1}} \left(f_{w,i}^{\tau_2} \frac{\partial x_l^{\tau_1}}{\partial x_i^{\tau_2}} det(F) - f_{w,l}^{\tau_1} \right) d\Omega^{\tau_1} = -\Delta_3^{\tau_1} \tag{16}$$

$$\int_{\Omega^{\tau_1}} T^* \left(\dot{S}_T^{\tau_2} det(F) - \dot{S}_T^{\tau_1} \right) - \frac{\partial T^*}{\partial x_l^{\tau_1}} \left(f_{T,i}^{\tau_2} \frac{\partial x_l^{\tau_1}}{\partial x_i^{\tau_2}} det(F) - f_{T,l}^{\tau_1} \right) d\Omega^{\tau_1} = -\Delta_4^{\tau_1} \tag{17}$$

where $det(F)$ is Jacobian determinant of the transformation matrix between the two configurations:

$$det(F) = \left| \frac{\partial x_i^{\tau_2}}{\partial x_j^{\tau_1}} \right| \approx 1 + \frac{\partial du_i^{\tau_1}}{\partial x_i^{\tau_1}} \tag{18}$$

The variations between Ω^{τ_2} and Ω^{τ_1} are defined as follows:

$$du_i^{\tau_1} = x_i^{\tau_2} - x_i^{\tau_1} \tag{19}$$
$$dp_w^{\tau_1} = p_w^{\tau_2} - p_w^{\tau_1} \tag{20}$$
$$dT^{\tau_1} = T^{\tau_2} - T^{\tau_1} \tag{21}$$
$$dv_{ij}^{\tau_1} = v_{ij}^{\tau_2} - v_{ij}^{\tau_1} \tag{22}$$
$$d\lambda_i^{\tau_1} = \lambda_i^{\tau_2} - \lambda_i^{\tau_1} \tag{23}$$
$$d\sigma_{ij}^{\tau_1} = \sigma_{ij}^{\tau_2} - \sigma_{ij}^{\tau_1} = d\sigma_{ij}'^{\tau_1} - b dp_w^{\tau_1} \delta_{ij} \tag{24}$$
$$d\Sigma_{ijk}^{\tau_1} = \Sigma_{ijk}^{\tau_2} - \Sigma_{ijk}^{\tau_1} \tag{25}$$
$$d\phi^{\tau_1} = (b - \phi^{\tau_1}) \left(\frac{\partial du_m^{\tau_1}}{\partial x_m^{\tau_1}} + \frac{1}{K_s} dp_w^{\tau_1} - \alpha_d dT^{\tau_1} \right) \tag{26}$$

$$d\rho_w^{\tau_1} = \rho_w^{\tau_2} - \rho_w^{\tau_1} = \rho_w^{\tau_1}\left(\frac{dp_w^{\tau_1}}{\chi_w} - \alpha_w^{\tau_1} dT^{\tau_1}\right) \tag{27}$$

$$d\rho_s^{\tau_1} = \rho_s^{\tau_2} - \rho_s^{\tau_1} = \rho_s^{\tau_1}\left[\frac{b-\phi^{\tau_1}}{(1-\phi^{\tau_1})K_s} dp_w^{\tau_1} - \frac{b-\phi^{\tau_1}}{1-\phi^{\tau_1}}\alpha_d dT^{\tau_1} - \frac{1-b}{1-\phi^{\tau_1}}\frac{d\Omega^{\tau_1}}{\Omega^{\tau_1}}\right] \tag{28}$$

The balance equations are rewritten in a matricial form for the purpose of the definition of local element stiffness matrix:

$$\int_{\Omega^{\tau_1}} \left[U_{(x,y)}^{*,\tau_1}\right]^T [E^{\tau_1}] \left[dU_{(x,y)}^{\tau_1}\right] d\Omega^{\tau_1} = -\Delta_1^{\tau_1} - \Delta_2^{\tau_1} - \Delta_3^{\tau_1} - \Delta_4^{\tau_1} \tag{29}$$

The thermal effects are introduced into the matrices $\left[U_{(x,y)}^{*,\tau_1}\right]$, $[E^{\tau_1}]$ and $\left[dU_{(x,y)}^{\tau_1}\right]$ based on Collin et al. (2006). The definition of stiffness matrix reads:

$$E^{\tau_1} = \begin{bmatrix} E1_{(4\times4)}^{\tau_1} & 0_{(4\times2)} & K_{WM(4\times3)}^{\tau_1} & K_{TM(4\times3)}^{\tau_1} & 0_{(4\times8)} & 0_{(4\times4)} & -I_{(4\times4)} \\ G1_{(2\times4)}^{\tau_1} & 0_{(2\times2)} & G2_{(2\times3)}^{\tau_1} & G3_{(2\times3)}^{\tau_1} & 0_{(2\times8)} & 0_{(2\times4)} & 0_{(2\times4)} \\ K_{MW(3\times4)}^{\tau_1} & 0_{(3\times2)} & K_{WW(3\times3)}^{\tau_1} & K_{TW(3\times3)}^{\tau_1} & 0_{(3\times8)} & 0_{(3\times4)} & 0_{(3\times4)} \\ K_{MT(3\times4)}^{\tau_1} & 0_{(3\times2)} & K_{WT(3\times3)}^{\tau_1} & K_{TT(3\times3)}^{\tau_1} & 0_{(3\times8)} & 0_{(3\times4)} & 0_{(3\times4)} \\ E2_{(8\times4)}^{\tau_1} & 0_{(8\times2)} & 0_{(8\times3)} & 0_{(8\times3)} & D_{(8\times8)}^{\tau_1} & 0_{(8\times4)} & 0_{(8\times4)} \\ E3_{(4\times4)}^{\tau_1} & 0_{(4\times2)} & 0_{(4\times3)} & 0_{(4\times3)} & 0_{(4\times8)} & 0_{(4\times4)} & I_{(4\times4)} \\ E4_{(4\times4)}^{\tau_1} & 0_{(4\times2)} & 0_{(4\times3)} & 0_{(4\times3)} & 0_{(4\times8)} & -I_{(4\times4)} & 0_{(4\times4)} \end{bmatrix} \tag{30}$$

where the matrices $E1_{(4\times4)}^{\tau_1}$, $E2_{(8\times4)}^{\tau_1}$, $E3_{(4\times4)}^{\tau_1}$, $E4_{(4\times4)}^{\tau_1}$ and $D_{(8\times8)}^{\tau_1}$ are the same as the ones for monophasic medium detailed in Chambon and Moullet (2004). The full development of stiffness matrix is detailed in appendix A.

2.4 Validation of the thermo-poro-elastic framework

When the temperature is increasing in porous geomaterials, a paramount phenomenon is the significant rise of pore pressure due to thermal pressurisation (Ghabezloo et al., 2009; Ghabezloo and Sulem, 2010). The thermo-poro-elastic framework is recalled here, on the one hand, to represent the overpressure induced by thermal effects and to highlight the major role of some parameters. On the other hand, the numerical validation was carried out between the thermo-poro-elastic framework and the implemented THM model (in section 2.3).

The presented framework comes from the study of Ghabezloo et al. (2009) and Braun (2019) to describe the macroscopic thermo-elastic volumetric behaviour of a porous material. For a fully saturated material, the variation of pore volume is consistent with that of the fluid phase. The porosity ϕ is defined as the pore volume V_ϕ to the total volume V in the deformed state: $\phi = V_\phi/V$. An isotropic stress state is considered (positive in compression),

thus three independent parameters are introduced here to describe the volumetric response of the porous material: the Terzaghi effective stress σ_d, the pore pressure p_w and the temperature T.

The variation of material volume V and of pore volume V_ϕ are expressed as follow:

$$\frac{dV}{V} = \frac{1}{V}(\frac{\partial V}{\partial \sigma_d})_{p_w,T} d\sigma_d + \frac{1}{V}(\frac{\partial V}{\partial p_w})_{\sigma_d,T} dp_w + \frac{1}{V}(\frac{\partial V}{\partial T})_{\sigma_d,p_w} dT \tag{31}$$

$$\frac{dV_\phi}{V_\phi} = \frac{1}{V_\phi}(\frac{\partial V_\phi}{\partial \sigma_d})_{p_w,T} d\sigma_d + \frac{1}{V_\phi}(\frac{\partial V_\phi}{\partial p_w})_{\sigma_d,T} dp_w + \frac{1}{V_\phi}(\frac{\partial V_\phi}{\partial T})_{\sigma_d,p_w} dT \tag{32}$$

Six parameters within above formula can be introduced as:

$$\frac{1}{K_d} = -\frac{1}{V}(\frac{\partial V}{\partial \sigma_d})_{p_w,T} \qquad \frac{1}{K_p} = -\frac{1}{V_\phi}(\frac{\partial V_\phi}{\partial \sigma_d})_{p_w,T} \tag{33}$$

$$\frac{1}{K_s} = -\frac{1}{V}(\frac{\partial V}{\partial p_w})_{\sigma_d,T} \qquad \frac{1}{K_\phi} = -\frac{1}{V_\phi}(\frac{\partial V_\phi}{\partial p_w})_{\sigma_d,T} \tag{34}$$

$$\alpha_d = \frac{1}{V}(\frac{\partial V}{\partial T})_{\sigma_d,p_w} \qquad \alpha_\phi = \frac{1}{V_\phi}(\frac{\partial V_\phi}{\partial T})_{\sigma_d,p_w} \tag{35}$$

where K_d and K_p are the drained bulk modulus of a porous medium and their pore volumes respectively, K_s and K_ϕ are the unjacketed modulus of solid grains assembly and of the pore volume respectively. α_d and α_ϕ are the drained volumetric thermal expansion coefficient of the porous medium and pore volume respectively. For homogeneous and isotropic porous material, $K_s = K_\phi$ and $\alpha_d = \alpha_\phi = \alpha_s$ are adopted, where α_s is the the thermal expansion coefficient of the solid skeleton. It is assumed that the skeleton and pore volume experience a same volumetric strain without change of porosity. Using Betti's reciprocal theorem, the following expression can be obtained:

$$\frac{1}{K_p} = \frac{1}{\phi}(\frac{1}{K_d} - \frac{1}{K_s}) \tag{36}$$

Using Eq. 36, the variations of total volume V and of pore volume V_ϕ is rewritten as follows:

$$\frac{dV}{V} = -\frac{1}{K_d} d\sigma_d - \frac{1}{K_s} dp_w + \alpha_d dT \tag{37}$$

$$\frac{dV_\phi}{V_\phi} = -\frac{1}{K_p} d\sigma_d - \frac{1}{K_\phi} dp_w + \alpha_\phi dT \tag{38}$$

The incremental volumetric strain is expressed as:

$$d\epsilon = -\frac{dV}{V} = \frac{1}{K_d} d\sigma_d + \frac{1}{K_s} dp_w - \alpha_d dT \tag{39}$$

In the case of undrained condition, the following expression is obtained:

$$dm_w = d(\rho_w \cdot V_\phi) = d\rho_w \cdot V_\phi + \rho_w \cdot dV_\phi = 0 \tag{40}$$

where $d\rho_w = \rho_w(dp_w/\chi_w - \alpha_w dT)$. Inserting Eq. 36, 38 and 39 in Eq. 40, the following expression is obtained:

$$\frac{dp_w}{\chi_w} - \alpha_w dT = \frac{K_d}{K_p}(d\epsilon - \frac{dp_w}{K_s} + \alpha_d dT) + \frac{1}{K_\phi} dp_w - \alpha_\phi dT \tag{41}$$

The stress-strain-thermal relation can be rewritten as:

$$d\epsilon = C(d\sigma - b dp_w) - \alpha_d dT \tag{42}$$

where C is compliance tensor, $d\sigma$ is the incremental total stress. By inserting Eq. 42 in Eq. 41, the variation of pore pressure is characterised as follow:

$$dp_w = \frac{\phi(\alpha_w - \alpha_s)dT + bCd\sigma}{\frac{1}{M} + bCb} \tag{43}$$

$$\frac{1}{M} = \phi(\frac{1}{\chi_w} - \frac{1}{K_\phi}) + \frac{b}{K_s} \tag{44}$$

where M is the Biot modulus. It is worth mentioning that $bCd\sigma$ in Eq. 43 can be also extended to anisotropic case.

A simplified model is built to validate the consistency of pore pressure variation between analytical (Eq. 43) and numerical solutions. The model is performed with one element in undrained condition, and the normal displacements are constrained along the horizontal and vertical axes. The evolutions of total stress and temperature are imposed at the external boundary and at the nodes respectively, and successively. The aim is to represent their individual effect on the pore pressure variation. The anisotropic rock properties are defined with Table 1.

Fig. 3 and Fig. 4 display the variations of pore pressure with respect to the changes of total stress and temperature respectively. The pore pressure increases linearly due to the linear rise of total stress. A nonlinear relation between the pore pressure variation and temperature increase is captured, which is linked to the temperature dependency of water thermal dilation (Fig. 1). Good agreements of pore pressure variations are observed between the analytical and numerical results.

3 Constitutive Model

Constitutive model and their parameters are introduced to model the THM coupling around the EDZ. Under fully saturated condition, the classical mechanical law and the second gradient constitutive model are presented in this section.

Table 1 THM parameters for the Callovo-Oxfordian claystone

	Symbol	Name	Value	Unit
Elastic	ρ_s	Solid phase density	2690	kg/m^3
	$E_\parallel$	Young's modulus parallel to bedding	8000	MPa
	$E_\perp$	Young's modulus normal to bedding	5000	MPa
	$\nu_{\parallel\parallel}$	Poisson's ratio parallel to bedding	0.21	-
	$\nu_{\parallel\perp}$	Poisson's ratio normal to bedding	0.35	-
	$G_\perp$	Shear modulus normal to bedding	2500	MPa
	$b_\parallel$	Parallel Biot's coefficient	0.83	-
	$b_\perp$	Perpendicular Biot's coefficient	0.87	-
Plastic	η	Van Eekelen yield surface convexity parameter	-0.229	-
	$\psi_c = \psi_E$	Dilatancy angles	0.5	$^\circ$
	$\phi_{c,0}$	Initial compression friction angle	10	$^\circ$
	$\phi_{c,f}$	Final compression friction angle	23	$^\circ$
	$\phi_{E,0}$	Initial extension friction angle	7	$^\circ$
	$\phi_{E,f}$	Final extension friction angle	23	$^\circ$
	B_ϕ	Friction angle hardening coefficient	0.001	-
	B_c	Cohesion softening coefficient	0.003	-
	$\bar{c}$	Cohesion for isotropic loading	4.1	MPa
	$A_\parallel$	Cohesion parameter	0.117	-
	b_1	Cohesion parameter	14.24	-
Hydraulic	$k_\parallel$	Intrinsic permeability parallel to bedding	$3.9E^{-20}$	m^2
	$k_\perp$	Intrinsic permeability normal to bedding	$1.3E^{-20}$	m^2
	ϕ	Porosity	0.18	-
	χ_w^{-1}	Water compressibility	$4.5E^{-4}$	MPa^{-1}
	ρ_w	Water density	1000	kg/m^3
Thermal	c_s	Solid phase specific heat	790	$J/kg/K$
	α_s	Linear thermal expansion coefficient	$1.25E^{-5}$	K^{-1}
	c_w	Water specific heat	4180	$J/kg/K$
	$\lambda_\parallel$	Thermal conductivity parallel to bedding	1.88	$W/m/K$
	$\lambda_\perp$	Thermal conductivity normal to bedding	1.25	$W/m/K$

3.1 First gradient mechanical law

The classical mechanical law is a non-associated elastoplastic model with linear elasticity and a Van Eekelen criterion (VE), which consists of a smoothing of the Mohr Coulomb plasticity surface (Fig. 5). The yield formulation (Van Eekelen, 1980) reads:

$$II_{\hat{\sigma}} + m\left(I_\sigma - \frac{3c}{\tan\phi_c}\right) = 0 \tag{45}$$

where I_σ is the first stress invariant, $II_{\hat{\sigma}}$ is the second deviatoric stress invariant, c is the cohesion, ϕ_c is the friction angle in compression, m is a parameter of the yield surface defined as follow:

$$m = a(1 + bsin3\beta)^\eta \tag{46}$$

where β is the Lode angle given by:

$$\sin(3\beta) = -\frac{3\sqrt{3}}{2}\frac{III_{\hat{\sigma}}}{II_{\hat{\sigma}}^3} \tag{47}$$

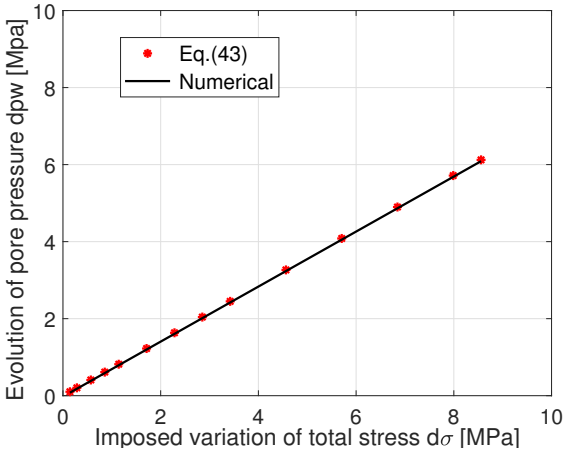

Fig. 3 Pore pressure evolution between the analytical and numerical results based on imposed total stress.

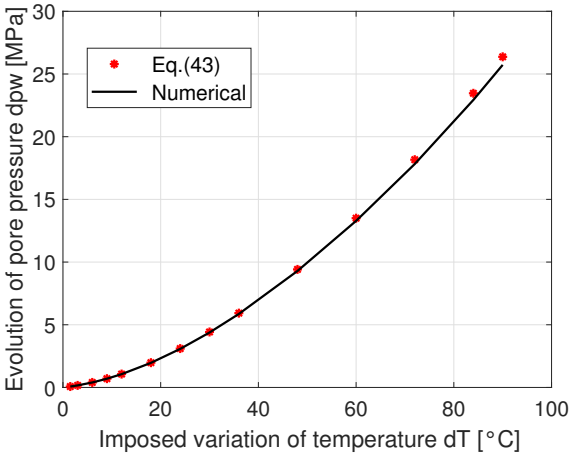

Fig. 4 Pore pressure evolution between the analytical and numerical results based on imposed temperature.

where $III_{\hat{\sigma}}$ is the third deviatoric stress invariant, a and b are the internal parameters related to the friction angles in compression and in extension, and the default value $\eta = -0.229$ is generally chosen to control the yield surface convexity.

The isotropic hardening and/or softening of friction angle and cohesion are considered as a function of Von Mises' equivalent plastic strain ϵ^p_{eq} which is defined as follow:

$$\epsilon^p_{eq} = \sqrt{\frac{2}{3}\hat{\epsilon}^p_{ij}\hat{\epsilon}^p_{ij}} \tag{48}$$

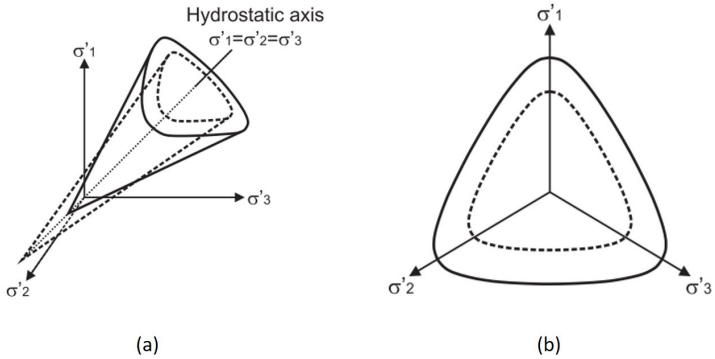

Fig. 5 Van Eekelen yield surface: (a) in the principal effective stress space, (b) in the deviatoric plane.

where $\hat{\epsilon}^p_{ij}$ is the deviatoric strain tensor determined by the plastic strain tensor ϵ^p_{ij}:

$$\hat{\epsilon}^p_{ij} = \epsilon^p_{ij} - \frac{\epsilon^p_{ii}}{3}\delta_{ij} \tag{49}$$

The functions of hardening/softening are introduced by an hyperbolic variation of the internal variables (Barnichon, 1998):

$$\phi_c = \phi_{c,0} + \frac{(\phi_{c,f} - \phi_{c,0})\epsilon^p_{eq}}{B_\phi + \epsilon^p_{eq}} \tag{50}$$

$$\phi_E = \phi_{E,0} + \frac{(\phi_{E,f} - \phi_{E,0})\epsilon^p_{eq}}{B_\phi + \epsilon^p_{eq}} \tag{51}$$

$$c = c_0 + \frac{(c_f - c_0)\epsilon^p_{eq}}{B_c + \epsilon^p_{eq}} \tag{52}$$

where c_0 and c_f are the initial and final cohesions, $\phi_{c,0}$ and $\phi_{c,f}$ are the initial and final compression friction angles, $\phi_{E,0}$ and $\phi_{E,f}$ are the initial and final extension friction angles, and the coefficients B_ϕ and B_c are the values of the equivalent plastic strain where half of the hardening/softening of friction angles and cohesion are reached (Fig. 6).

In this study, the selected host rock is Callovo-Oxfordian claystone, which is envisaged by the French national radioactive waste management agency (Andra) and holds strong cross-anisotropic material behaviour (Amadei, 2012). Fig. 7 describes the material (orthotropic) axes e_1, e_2, and e_3, which may be not consistent with the global axes x, y, and z. The cross-anisotropic material displays a certain type of symmetry with a symmetry axis (e_2) and an isotropic plane called bedding plane (e_1e_3) normal to the axis (Abelev and Lade, 2004; Lade, 2007). As a result, five independent parameters ($E_\parallel$, $E_\perp$, $\nu_{\parallel\parallel}$, $\nu_{\parallel\perp}$ and $G_{\parallel\perp}$) are requested to describe the cross-anisotropic elastic behaviour, and the compressibility of solid grains skeleton is introduced by anisotropic Biot coefficients ($b_\parallel$ and $b_\perp$), where the subscripts $\parallel$ and $\perp$ indicate the directions parallel

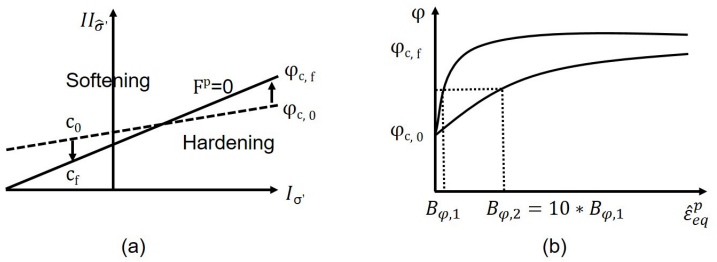

Fig. 6 Van Eekelen yield surface with hardening/softening: (a) in the stress invariant plane, (b) hyperbolic relation for two values of coefficient B_ϕ.

and normal to the bedding planes respectively. Additionally, plastic behaviour can be also anisotropic and be subjected to loading and material structure orientations. Numerous studies on yield surface variation for anisotropic materials have already been carried out (Lade, 2007; Jaeger, 1960; Hoek and Brown, 1980). Here cohesion anisotropy expressed by the fabric tensor concept is considered. A second order microstructure fabric tensor a_{ij} draws the spatial distribution of cohesion, where the subscripts i, j are corresponding to the principal material microstructure axes (e_1, e_2, and e_3). The cohesion is defined as the projection of the tensor on a unit loading vector l_i which denotes the loading direction relative to the principal material axes (Pietruszczak and Mroz, 2000, 2001; Chen et al., 2010). The component of l_i is determined by the stress resultant imposed on facets of normal axis e_i and reads:

$$l_i = \sqrt{\frac{{}^\sharp\sigma'^2_{i1} + {}^\sharp\sigma'^2_{i2} + {}^\sharp\sigma'^2_{i3}}{{}^\sharp\sigma'_{jk}\,{}^\sharp\sigma'_{jk}}} \tag{53}$$

where ${}^\sharp\sigma'_{jk}$ is given within the reference of material axes. The cohesion hence describes the effect of loading direction relative to material axes (Pietruszczak et al., 2002; Pietruszczak, 2010)):

$$c_0 = a_{ij} l_i l_j \tag{54}$$

By adopting the deviatoric part of microstructure tensor (Ken-Ichi, 1984):

$$c_0 = \overline{c}(1 + A_{ij} l_i l_j) \tag{55}$$

$$A_{ij} = \frac{\hat{a}_{ij}}{\overline{c}} = \frac{a_{ij}}{\overline{c}} - \delta_{ij} \tag{56}$$

$$\overline{c} = \frac{a_{ii}}{3} \tag{57}$$

where $\overline{c}$ is a microstructure parameter, A_{ij} is a traceless symmetric tensor, $A_{ii} = 0$, and $\hat{a}_{ij} = a_{ij} - \frac{a_{kk}}{3}\delta_{ij}$ is the deviatoric part of the microstructure

tensor. The higher order tensors are taken into account within Eq. 55:

$$c_0 = \bar{c}\left(1 + A_{ij}l_il_j + b_1(A_{ij}l_il_j)^2 + b_2(A_{ij}l_il_j)^3 + \cdots\right) \tag{58}$$

where b_1, b_2,... are constants. Within the material axes, $A_{ij} = 0$ for $i \neq j$ with $A_{ii} = A_{11} + A_{22} + A_{33} = 0$ is denoted, and the projection of A_{ij} on the loading vector reads:

$$A_{ij}l_il_j = A_{11}l_1^2 + A_{22}l_2^2 + A_{33}l_3^2 \tag{59}$$

Assuming that an isotropic stress state is applied, where $l_1 = l_2 = l_3 = \sqrt{1/3}$ by Eq. 53 leads to $A_{ij}l_il_j = A_{ii}/3 = 0$ by Eq. 56 and 59, and to $c_0 = \bar{c}$ by Eq. 55, hereafter $\bar{c}$ is the cohesion under isotropic loading. For cross-anisotropy, $A_{11} = A_{33} = A_{\parallel}$ and $A_{22} = -2A_{11} = -2A_{\parallel}$ are implied if the bedding planes are parallel to (e_1, e_3), where $A_{\parallel}$ is the component of microstructure tensor A_{ij} in the bedding planes. Accordingly:

$$A_{ij}l_il_j = A_{\parallel}(1 - 3l_2^2) \tag{60}$$

where l_2 is the component of l_i acting on the facet parallel to the bedding planes. The Eq. 58 can be rewritten as:

$$c_0 = \bar{c}\left(1 + A_{\parallel}(1 - 3l_2^2) + b_1A_{\parallel}^2(1 - 3l_2^2)^2 + b_21A_{\parallel}^3(1 - 3l_2^2)^3 + \cdots\right) \tag{61}$$

The constants $\bar{c}$, $A_{\parallel}$, b_1, b_2, ... can be acquired from experimental data. It is worth mentioning that the evolution of cohesion is both dependent on the material fabric and to the loading, hence it is more convenient to define a final cohesion c_f using $c_f = \xi c_0$, where ξ is the ratio of cohesion softening.

3.2 Second gradient mechanical law

The second gradient model is introduced to define the constitutive relation between double stress and microkinematics. Assuming the microkinematic gradient is only relevant to mechanical part, the second gradient law can be decoupled with classical mechanic law appropriately. A linear isotropic

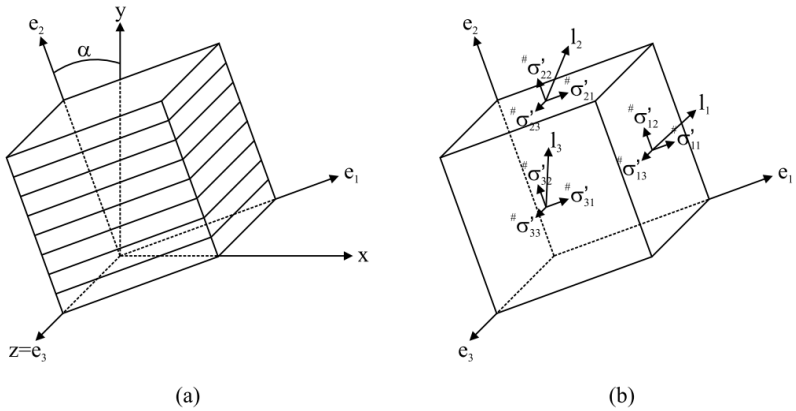

Fig. 7 Principal axes for cross-anisotropy material: (a) rotation of the bedding plane, (b) stress state in the material axes configuration and loading vectors.

relationship is derived for simplicity from Mindlin (1965):

$$\begin{bmatrix} \tilde{\Sigma}_{111} \\ \tilde{\Sigma}_{112} \\ \tilde{\Sigma}_{121} \\ \tilde{\Sigma}_{122} \\ \tilde{\Sigma}_{211} \\ \tilde{\Sigma}_{212} \\ \tilde{\Sigma}_{221} \\ \tilde{\Sigma}_{222} \end{bmatrix} = D \begin{bmatrix} 1 & 0 & 0 & 0 & 0 & \frac{1}{2} & \frac{1}{2} & 0 \\ 0 & \frac{1}{2} & \frac{1}{2} & 0 & -\frac{1}{2} & 0 & 0 & \frac{1}{2} \\ 0 & \frac{1}{2} & \frac{1}{2} & 0 & -\frac{1}{2} & 0 & 0 & \frac{1}{2} \\ 0 & 0 & 0 & 1 & 0 & -\frac{1}{2} & -\frac{1}{2} & 0 \\ 0 & -\frac{1}{2} & -\frac{1}{2} & 0 & 1 & 0 & 0 & 0 \\ \frac{1}{2} & 0 & 0 & -\frac{1}{2} & 0 & \frac{1}{2} & \frac{1}{2} & 0 \\ \frac{1}{2} & 0 & 0 & -\frac{1}{2} & 0 & \frac{1}{2} & \frac{1}{2} & 0 \\ 0 & \frac{1}{2} & \frac{1}{2} & 0 & 0 & 0 & 0 & 0 \end{bmatrix} \begin{bmatrix} \frac{\partial \dot{v}_{11}}{\partial x_1} \\ \frac{\partial \dot{v}_{11}}{\partial x_2} \\ \frac{\partial \dot{v}_{12}}{\partial x_1} \\ \frac{\partial \dot{v}_{12}}{\partial x_2} \\ \frac{\partial \dot{v}_{21}}{\partial x_1} \\ \frac{\partial \dot{v}_{21}}{\partial x_2} \\ \frac{\partial \dot{v}_{22}}{\partial x_1} \\ \frac{\partial \dot{v}_{22}}{\partial x_2} \end{bmatrix} \tag{62}$$

where D is the constitutive elastic modulus, representing the physical microstructure and characterising the internal length scale for the width of shear band (Chambon et al., 1998), $\dot{v}_{ij}$ is the time derivative of v_{ij}, and $\tilde{\Sigma}_{ijk}$ is the Jaumann double stress rate (Collin et al., 2006):

$$\tilde{\Sigma}_{ijk} = D_{ijklmn} \frac{\partial \dot{v}_{lm}}{\partial x_n} = \dot{\Sigma}_{ijk} + \Sigma_{ljk}\omega_{li} + \Sigma_{imk}\omega_{mj} + \Sigma_{ijp}\omega_{pk} \tag{63}$$

where $\dot{\Sigma}_{ijk}$ is the time derivative of Σ_{ijk}, and ω_{ij} is the spin tensor.

4 Numerical applications

A 2D plane strain model (Fig. 8) considering thermo-hydro-mechanical coupling effects has been used, based on the Eurad Hitec (2019) benchmark exercise. The geometry of this model is a cross-section of a heating drift in the host rock. Only a quarter of the full drift is modelled thanks to the symmetry of the problem and the boundary conditions. The radius of the drift wall

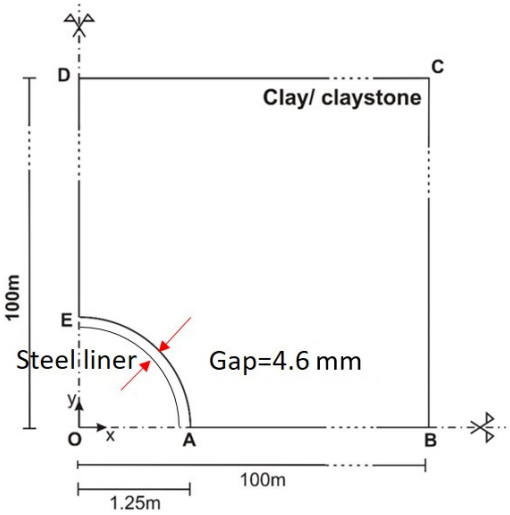

Fig. 8 Model geometry for the near-field case

is 1.25 m with an extension of 100 m to the external boundary, and the discretisation is performed with 22923 nodes and 5760 elements. The mesh is well refined close to the drift wall to get a better reproduction of rock behaviour in the EDZ. A steel liner is modelled to avoid large deformation of the drift wall. The gap between the drift wall and the liner is defined as 4.6 mm. The gap value is in accordance with the numerical prediction of the average deformation of the drift wall at the end of excavation, when there is no liner imposed. The numerical application is performed with the finite element code Lagamine developed at University of Liège. It is worth mentioning that, the radius of 1.25 m is not the size of French high level waste (HLW) concept, but only a proposed benchmark in the EURAD Hitec project. The steel liner in the simulation is simply modelled by an infinitely rigid element in the code.

The Callovo-Oxfordian claystone (COx) is selected as a candidate host formation due to its low permeability and good plasticity, and the detailed properties of COx can be found in Seyedi et al. (2021). The thermo-hydro-mechanical parameters come from the Hitec specification. The mechanical, hydraulic and thermal parameters are presented in Table 1, and Fig. 9 presents the evolution of the cohesion as a function of a fabric tensor as explained in section 3.1 (Pardoen et al., 2015b).

The initial anisotropic stress state, pore pressure and temperature are defined as follow:

$$\begin{aligned} p_{w,0} &= 4.7MPa \\ T_0 &= 22°C \\ \sigma_{x,0} &= 12.4MPa \\ \sigma_{y,0} &= 12.7MPa \end{aligned}$$

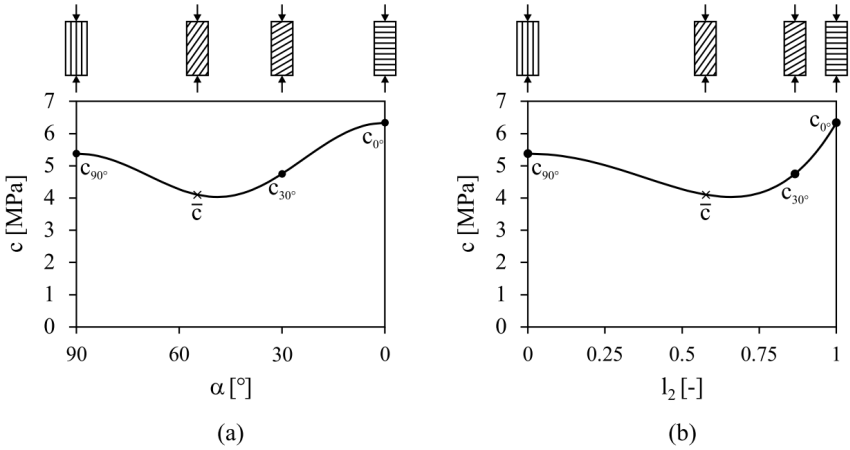

Fig. 9 Evolution of the cohesion (a) as a function of the angle between the normal to the bedding planes and the direction of loading and (b) as a function of the loading vector.

$$\sigma_{z,0} = 16.4MPa$$

where $p_{w,0}$ is the initial pore pressure, T_0 is the initial temperature, $\sigma_{y,0}$ is the vertical principal total stress, $\sigma_{z,0}$ is the major horizontal principal total stress, $\sigma_{x,0}$ is the minor horizontal principal total stress. The initial stresses, pore pressure and temperature are also imposed at the external boundary, where permeable boundary is applied. The drift wall is oriented in the direction of major horizontal principal stress, and the gravity effect is not considered in the modelling.

Considering the symmetry conditions, the normal displacements are constrained along the symmetry axes, where an impervious and an adiabatic boundary are defined to avoid the water flow and thermal flow. Additional kinematics boundary conditions with the case of 2^{nd} gradient model are also considered for symmmetry (Zervos et al., 2001b). It requires the radial displacement u_r should keep symmetric on both sides of symmetry axes, which means the normal derivative of u_r with respect to tangential direction θ has to cancel. The definition of the second gradient boundary aims to reproduce the evolution of strain localisation similar to the full-drift results, also for the reason of simulation simplicity. (Pardoen et al., 2015a).

To well reproduce the strain localisation, proper definition of internal length scale of second gradient law is of paramount importance. As referred in section 3.2, the internal length scale is charaterised with the D value of second gradient law, which is mesh independent (Collin et al., 2006). The value of $D = 15000N$ is applied in the following modelling.

The full computation is characterised by three phases: excavation (T0 - T0+24 h), waiting (T0+24 h - T0+180 days) and heating (T0+180 days - T0+10 years), conducted by adjusting boundary conditions of drift wall (Fig.

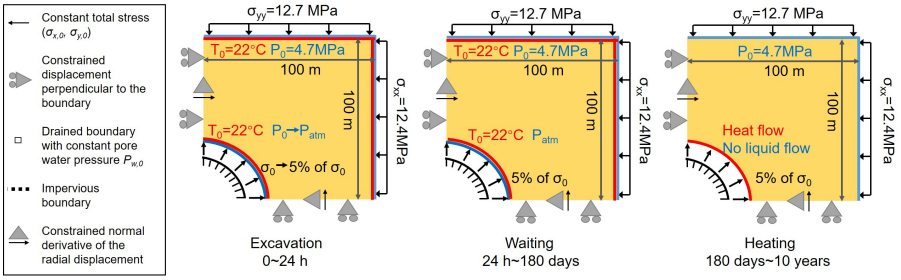

Fig. 10 Adjusting boundary conditions at the drift wall

10). To model the drift excavation, a stress release technique is used and the total stress at the drift wall decreases to 5% of the initial value. The pore pressure at the drift wall is reduced to the atmospheric pressure (0.1 MPa). The boundary conditions keep constant during the waiting phase. During the heating phase, a constant power (200 W/m) thermal flow is applied, as well as the undrained boundary at the wall.

The objective of this numerical modelling is to investigate the thermal effects on the rock in the EDZ, to reproduce the fracturation process involved with shear strain localisation.

5 Numerical Results

5.1 Evolution of temperature, pore pressure and convergence

The numerical results of temperature, pore pressure and convergence are presented at the points 1.25 m, 1.9 m, 2.5 m, 6.25 m, 50 m, and 100 m horizontally and vertically, plus 1.25 m, 1.9 m, 2.5 m at 45 degrees (OB, OD and OC directions in Fig. 8). The evolution of temperature, pore pressure and convergence are presented in Fig. 11, Fig. 12, Fig. 13.

During excavation and waiting steps, the temperature keeps constant as no thermal flow is imposed. The pore pressure at the drift wall decreases as defined with boundary condition during excavation, from 4.7 MPa to atmospheric pressure. The overpressure in horizontal direction is observed at the end of excavation, while the pore pressure in vertical direction continues to decrease in this stage. This discrepancy is due to the hydro-mechanical behaviour induced by anisotropic properties. The stabilisation of pore pressure is noticed during waiting. The host rock close to the wall experiences an increase of radial displacement during excavation, and the first contact between the wall and the liner is located at 45 degrees direction. The second contact is also reached during waiting in the vertical direction.

When the heating starts, the temperature increase is observed in the near field, and the excess pore pressure is highly pronounced due to the thermal pressurization. The maximum of temperature is located at the drift wall with about 80°C after 10 years. Inside the rock structure, the different distribution

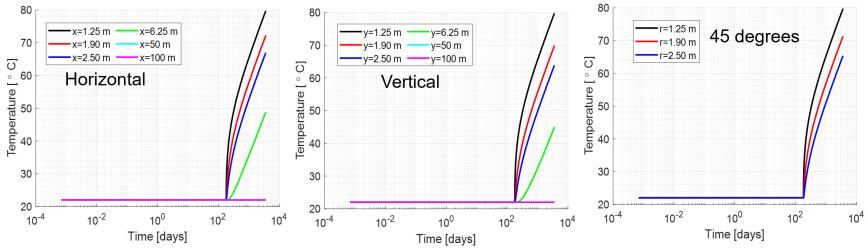

Fig. 11 Evolution of temperature at different locations

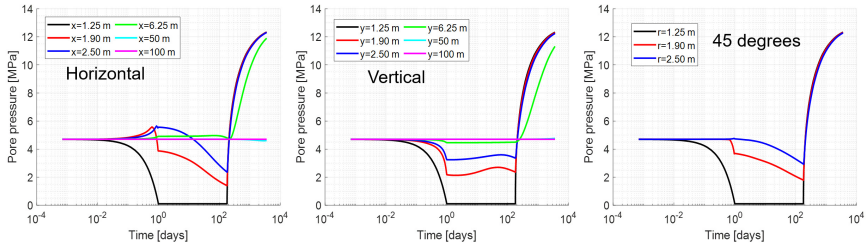

Fig. 12 Evolution of pore pressure at different locations

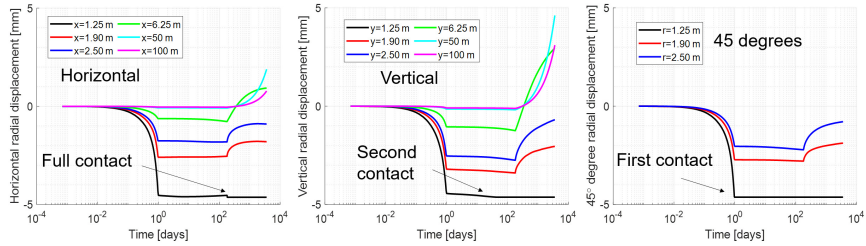

Fig. 13 Evolution of radial displacement at different locations

of temperature is evidenced due to the anisotropy of thermal conductivity. The higher temperature values are observed in the horizontal direction with a higher thermal conductivity. This difference also leads to the variation of pore pressure, which is consistent with Eq. 43. The pore pressure at 6.25 m in horizontal direction is slightly higher than that in vertical direction, while the pore pressure at the wall are the same due to the same amount of received thermal power. The full contact is obtained rapidly around the wall after the start of heating. The radial displacement decreases due to the thermal dilation of the host rock close to the wall, and the thermal expansion is more pronounced vertically than horizontally. For the location far from the wall, the temperature and pore pressure changes are not observed, and the modification of radial displacement is related to the accumulation of the thermal dilation from the nearfield rock.

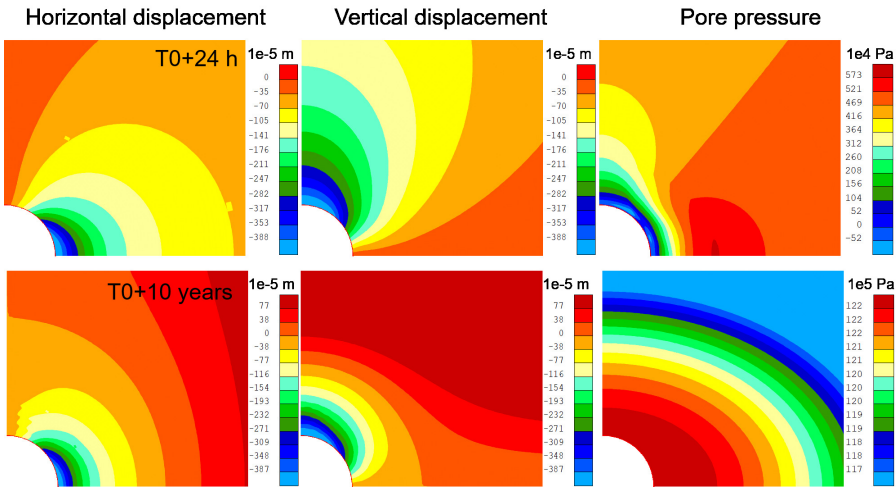

Fig. 14 Distribution of horizontal displacement, vertical displacement, and pore pressure at the end of excavation and heating

Since the material anisotropy is one of the principal features in the benchmark of THM coupling problem, Fig. 14 (in $5m \times 5m$ scale) shows the distribution of horizontal displacement, vertical displacement, and pore pressure at the end of excavation and heating. In the vertical direction after 24h, the displacements are observed deeper into the rock mass with respect to the horizontal direction. At the drift wall, the rigid liner imposes the same displacement in both directions. At the end of the heating, vertical extension due to thermal dilation is more evidenced than in the horizontal direction. Negative pore pressure is predicted close to the drift wall due to hydro-mechanical couplings at the end of excavation. An overpressure peak is clearly evidenced in the horizontal direction at the end of excavation, due to the anisotropy. At the end of heating, the overpressure is more pronounced horizontally due to a higher thermal conductivity in this direction.

5.2 Stress path

The stress paths are plotted to display the stress response during the excavation, waiting and heating phases. The description of stress paths of the rock at 1 R, 1.5 R and 2 R is of particular interest in Fig. 15. Globally, the rock behaviour firstly develops into plastic regime during excavation (24 hours), then it undergoes an unloading process back to elasticity during waiting (180 days). The decrease of total stress and pore pressure at the wall leads to stress redistribution during excavation, and the anisotropic properties of rock induce opposite variation of stress path during excavation and waiting. Once the heating starts, the rock behaviour becomes rapidly plastic again. The tensile stress at the wall is especially pronounced at the end of heating, and the maximum tensile stress is located at 45 degrees direction. It should be mentioned that, the strain localisation can also affect the rock behaviour. With the initiation

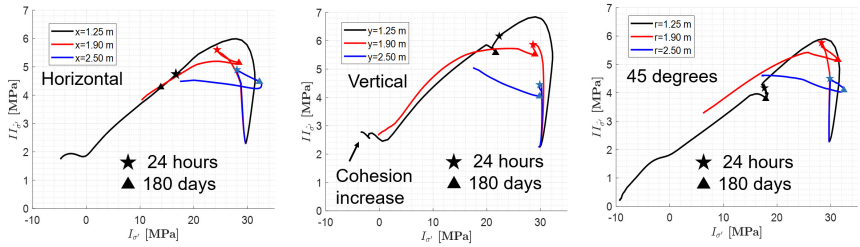

Fig. 15 Evolution of stress path at different locations

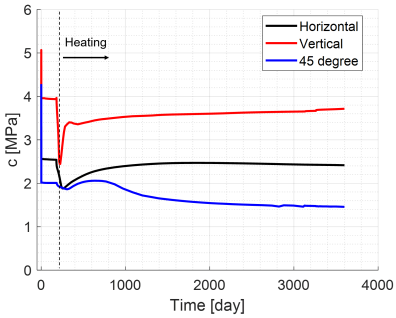

Fig. 16 Evolution of cohesion at the wall

and disappearance of shear bands, the rock behaviour can switch between the elasticity and plasticity, which will be discussed in the following section.

In addition, the dependency of stress paths on the variation of cohesion is clearly evidenced. Fig. 16 shows the evolution of cohesion at the wall, and it is affected significantly by the variation of loading directions caused by large deformation, thus it may get an increase even if the plastic softening is introduced. At the end of heating, the curve of stress paths at the wall move slightly up due to the increase of cohesion, and an apparent increase of cohesion in vertical direction leads to a distinct variation of stress path from other directions. The minimum cohesion is located at 45 degrees direction at all times, which is not surprising knowing that the first contact between the wall and liner is reached here.

5.3 Strain localisation

In this section, the evolution of shear strain localisation process is described in $3m \times 3m$ scale in Fig. 17, and the numerical results are plastic points, the deviatoric strain increment and the total deviatoric strain. Due to a lower cohesion as referred in Fig. 16, the host rock in 45 degrees direction gets the first contact with the liner, where the deformation is limited. Meanwhile, the horizontal and vertical convergence continues to develop, leading to an elastic zone located at the 45 degrees of the drift wall at the end of the excavation. The deviatoric strain increment also evidences the existence of the elastic zone. An

elastic unloading process is predicted due to the continuous drainage during the waiting phase. The strain localisation process is less active during this phase, and the total deviatoric strain keeps constant as well.

Once the heating phase is activated, the rock behaviour in EDZ comes to plasticity rapidly, and the shear bands are more pronounced than during excavation. The competition between different emerging shear bands is witnessed at the initial heating stage, and the bands are slightly more oriented along the minor horizontal principal stress direction, which is in agreement with the *in-situ* observation of localisation induced by the excavation process (Armand et al., 2014). It is worth mentioning that the initiation of the new shear bands does not follow the existing previous bands generated during the excavation. It illustrates that thermal effects strongly dominate the development of shear bands, neglecting the previous existing bands from excavation.

At the end of the heating phase, the competition between different emerging shear bands ends up with the domination of horizontal shear bands. The vertical shear bands are also visible in the total deviatoric strain, but they are not much developed as in the horizontal ones. In addition, the effect of strain localisation process on the rock behaviour in EDZ is also evidenced in Fig. 17. When a shear bands initiates, the stress state inside the band is purely localised in plasticity, the rock structure outside the band undergoes an elastic unloading process. At 360 days, the shear bands development is more observed horizontally in the upper half area, thus the stress state of the rock at the upper half wall consist of both elasticity (outside the bands) and plasticity (inside the bands). At 4 years, due to the initiation of a vertical shear band, the stress state at the upper half wall is almost in elasticity. At 10 years, the shear bands are developed horizontally due to thermal loading, hence some locations at the wall are back to plasticity again. With the initiation and disappearance of shear bands, the rock behaviour can be switched between plasticity and elasticity during heating.

Fig. 18 shows the evolution in horizontal and vertical normalized extensions of plastic zone (current extension/extension at 24 h) versus time. The increase of the normalized extensions of plastic zone is highly pronounced at the beginning of heating. However, this increasing rate of extensions decreases versus time. Finally, the extension of plastic zone keeps constant after 5 years of heating. It is interesting to see, the final plastic zone in horizontal direction is identical to the end of excavation, while it is 1.5 times larger than the plastic zone at the end of excavation in vertical direction.

6 Impact of the gap on the strain localisation process

In real *in-situ* construction, a liner is usually constructed to limit the convergence of the drift wall. Fig. 17 shows that the liner can affect the development of the localisation pattern in EDZ. In order to better understand the gap effect

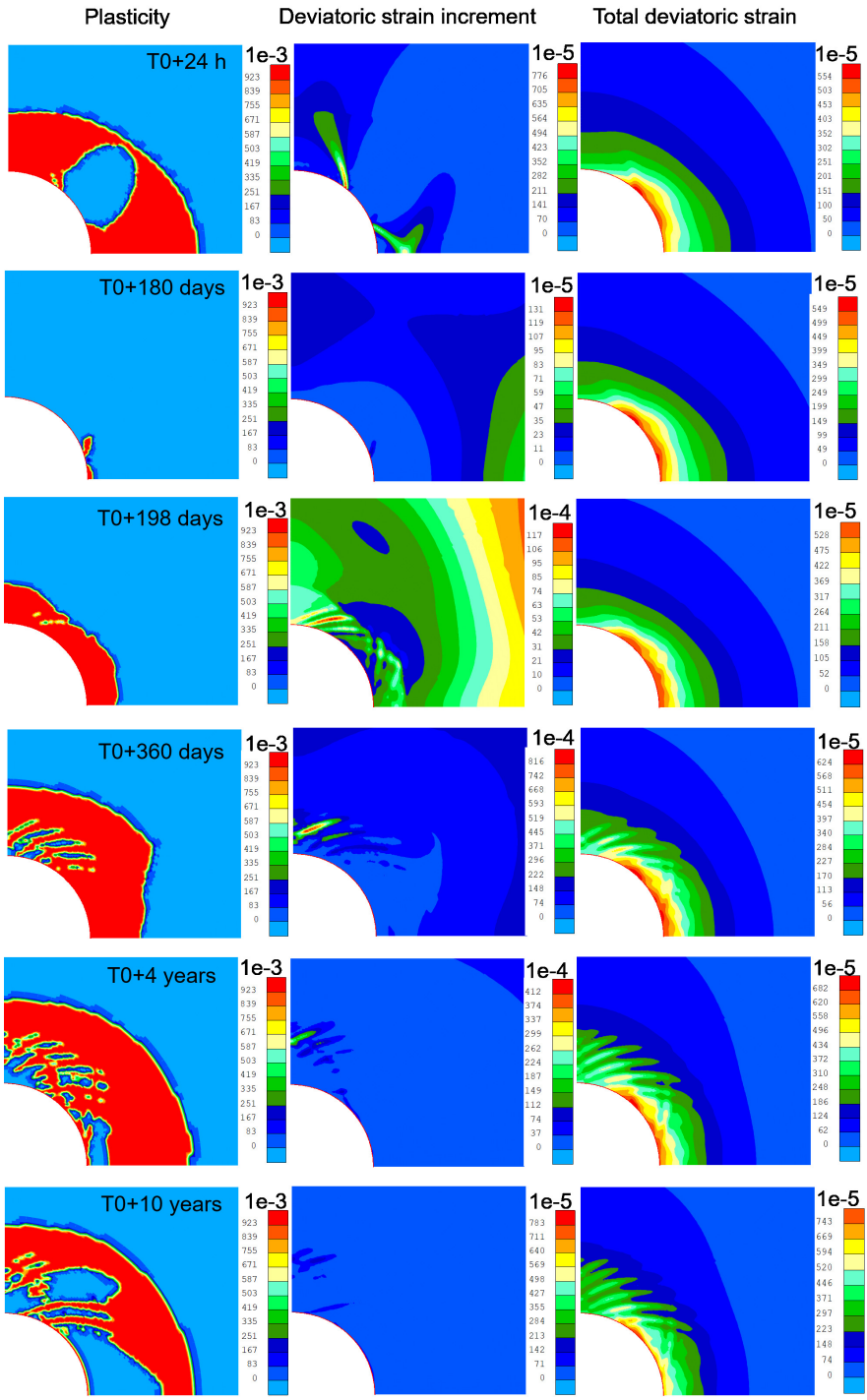

Fig. 17 Evolution of plastic points, deviatoric strain increment and total deviatoric strain around the EDZ

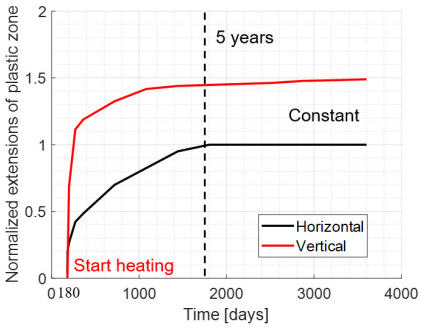

Fig. 18 Normalized extensions of the plastic zone: current extension/extension at 24 h.

on the EDZ development during the heating phase, three gap values are considered in the numerical investigations: 4.6 mm, 5.8 mm and infinite gap (no liner). 5.8 mm is actually the average predicted displacement of the drift wall at the end of waiting phase, when no liner is imposed.

Fig. 19 shows the evolution of the plastic points, deviatoric strain increment and total deviatoric strain at 237 days in $3m \times 3m$ scale. With an increasing gap, the plastic area becomes larger, and the strain localisation is gradually more pronounced. When the gap is equal to $4.6mm$, there are not many shear bands initiated from the drift wall. With a gap of $5.8mm$, the horizontal shear bands close to the wall are clearly observed. When there is no liner, the localised horizontal shear bands are highly pronounced. Such kind of phenomenon can be also observed in the evolution of total deviatoric strain. When the gap is infinite, the magnitude of total deviatoric strain is ten times higher than that of gap= $4.6mm$, and the shear bands are more localised with the increase of gap.

The gap effect on the rock behaviour can be explained through the contact situation between the wall and the liner. Fig. 20 (in $3m \times 3m$ scale) describes the different contact situation between the wall and liner for a gap respectively of $4.6mm$ and $5.8mm$, where the red diagram is the contact pressure. The contact process for gap= $4.6mm$ is consistent with the evolution of radial displacement in section 5. However, for the gap equal to $5.8mm$, only few elements in 45 degrees direction get contact with the liner at the end of waiting phase. No full contact is reached yet after 237 days, and the contact is not homogeneously distributed along the wall. Compared to Fig. 19, the strain localisation is less developed when the full contact is reached. Nonetheless, the shear bands are preferable to develop when the contact situation is poor. The shear bands are more pronounced in upper half area where no contact is obtained, which also evidences the mechanism. Considering the case without liner, the strain localisation can develop without any restriction, hence the shear bands are much more localised.

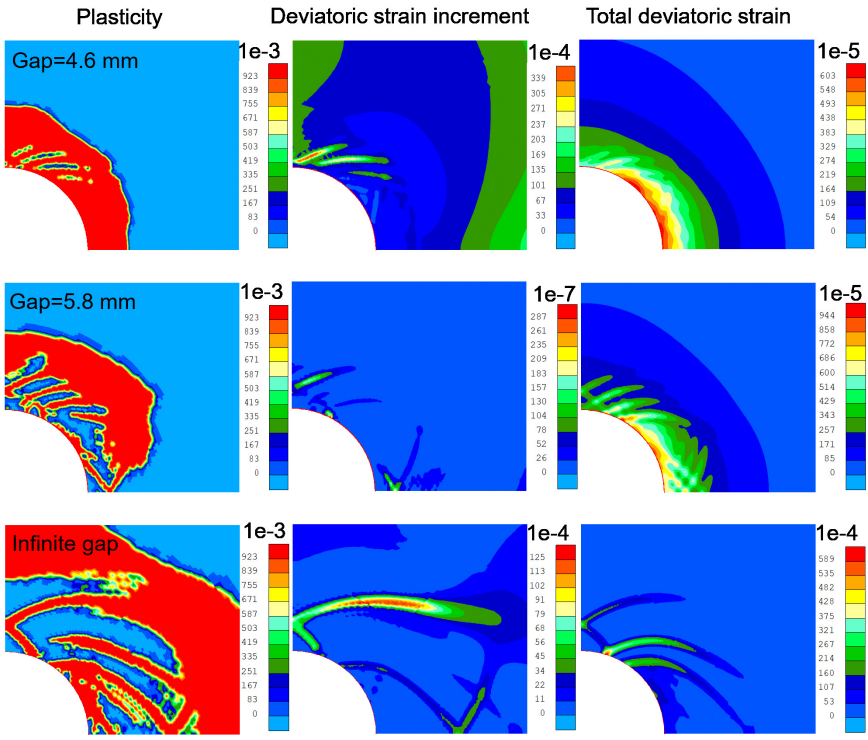

Fig. 19 Evolution of plastic points, deviatoric strain increment and total deviatoric strain at 237 days for different gap values.

7 Conclusion

A 2^{nd} gradient model for thermo-hydro-mechanical couplings is presented in this paper. The fully coupled nonlinear set of equations and the stiffness matrix are well built in the updated Lagrange configuration. This model is implemented based on the existing classical model in Lagamine to well reproduce the strain localisation induced by the thermal effects.

Thermo-poro-elasticity framework is summarised and allows the validation of the implemented model. Good agreements are obtained between the analytical and numerical results. The excess pore pressure induced by the variation of confining stress and temperature is evidenced, where the discrepancy of thermal dilation coefficient between solid and fluid phases is the root reason leading to overpressure.

Thereafter, the strain localisation induced by thermal effects is analysed. During the heating phase, the development of plasticity and strain localisation are highly pronounced. The shear bands are preferential to develop in the minor horizontal principal stress direction, which is consistent with the *in-situ* observations from excavation. The extension of plastic zone due to heating is limited, which is almost constant after 5 years of heating in this study.

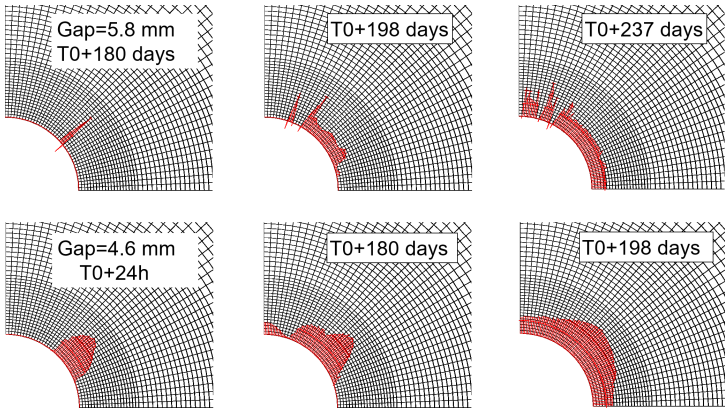

Fig. 20 Contact situation between the drift wall and liner for different gap values.

Finally, the effect of gap between the drift wall and liner on the rock behaviour is discussed. On the one hand, the strain localisation pattern around EDZ can be less developed when the gap is smaller. The initiation of shear bands is limited by the kinematic restriction from the liner. On the other hand, the shear bands are more localised with the increasing gap.

The plastic effect on thermal and hydraulic behaviour is limited in this study. The thermal conduction is mainly dependent on the thermal conductivity of the rock, which is considered as constant. The thermal convection is not highly pronounced in this study due to limited water flows (induced by the low permeability value). A dilatancy angle of 0.5 degrees is considered in this simulation. Therefore, the plastic volumetric deformation is limited and it will slightly affect the pore pressure. Additionally, the thermal effect on the thermal compaction, creep behaviour, and potential strength modification of the rock is not enclosed in this study. To enhance the coupling effect between plastic and hydraulic behaviour, the dependency of permeability on the plastic deformation (especially the shear band variation) will be introduced in future study. During the EURAD project, the numerical solution will be also qualified by comparing with the ongoing *in-situ* heating test (in future work).

Acknowledgments. This project has received funding from the European Union's Horizon 2020 research and innovation programme under grant agreement No 847593. The first author also would like to thank the China Scholarship Council (No.201906710096) for their financial support.

Author Contributions. Hangbiao Song: Conceptualization, investigation, methodology, software, validation, writing - original draft. Gilles Corman: Conceptualization, investigation, methodology, software, validation, writing. Frédéric Collin: Conceptualization, investigation, methodology, project administratio, writing - review and editing.

Declarations

The authors declare that they have no known competing financial interests or personal relationships that could have appeared to influence the work reported in this paper.

Appendix A Stiffness matrix

The stiffness matrix of the flow problem is:

$$K^{\tau_1}_{WW(3\times3)} = \begin{bmatrix} k_{11}\frac{\rho_w^{\tau_1}}{\mu_w^{\tau_1}} & k_{12}\frac{\rho_w^{\tau_1}}{\mu_w^{\tau_1}} & K_{WW_{1,3}} \\ k_{21}\frac{\rho_w^{\tau_1}}{\mu_w^{\tau_1}} & k_{22}\frac{\rho_w^{\tau_1}}{\mu_w^{\tau_1}} & K_{WW_{2,3}} \\ 0 & 0 & K_{WW_{3,3}} \end{bmatrix} \tag{A1}$$

where

$$K^{\tau_1}_{WW_{1,3}} = \frac{\rho_w^{\tau_1}}{\chi_w}\left[\frac{2\rho_w^{\tau_1}}{\mu_w^{\tau_1}}(k_{11}g_1 + k_{12}g_2) + \frac{1}{\mu_w^{\tau_1}}(k_{11}\frac{\partial p_w^{\tau_1}}{\partial x_1^{\tau_1}} + k_{12}\frac{\partial p_w^{\tau_1}}{\partial x_2^{\tau_1}})\right] \tag{A2}$$

$$K^{\tau_1}_{WW_{2,3}} = \frac{\rho_w^{\tau_1}}{\chi_w}\left[\frac{2\rho_w^{\tau_1}}{\mu_w^{\tau_1}}(k_{21}g_1 + k_{22}g_2) + \frac{1}{\mu_w^{\tau_1}}(k_{21}\frac{\partial p_w^{\tau_1}}{\partial x_1^{\tau_1}} + k_{22}\frac{\partial p_w^{\tau_1}}{\partial x_2^{\tau_1}})\right] \tag{A3}$$

$$\begin{aligned} K^{\tau_1}_{WW_{3,3}} = \rho_w^{\tau_1}\Bigg[&(\frac{\dot{p}_w^{\tau_1}}{\chi_w} - \alpha_w^{\tau_1}\dot{T}^{\tau_1} - \frac{\dot{p}_w^{\tau_1}}{K_s})(\frac{b-\phi^{\tau_1}}{K_s} + \frac{\phi^{\tau_1}}{\chi_w}) \\ &+ (\frac{\phi^{\tau_1}}{\chi_w \cdot \Delta t} + \frac{b-\phi^{\tau_1}}{K_s \cdot \Delta t}) + \frac{b}{\chi_w}(\frac{\dot{p}_w^{\tau_1}}{K_s} + \frac{\dot{\Omega}^{\tau_1}}{\Omega^{\tau_1}})\Bigg] \end{aligned} \tag{A4}$$

The stiffness of the thermal problem is:

$$K^{\tau_1}_{TT(3\times3)} = \begin{bmatrix} \lambda_s(1-\phi^{\tau_1}) + \lambda_w\phi^{\tau_1} & 0 & K_{TT_{1,3}} \\ 0 & \lambda_s(1-\phi^{\tau_1}) + \lambda_w\phi^{\tau_1} & K_{TT_{2,3}} \\ 0 & 0 & K_{TT_{3,3}} \end{bmatrix} \tag{A5}$$

where

$$\begin{aligned} K^{\tau_1}_{TT_{1,3}} = {} & \alpha_d(\lambda_s - \lambda_w)(b-\phi^{\tau_1})\frac{\partial T^{\tau_1}}{\partial x_1^{\tau_1}} - c_{p,w}\rho_w^{\tau_1} f_{w,1}^{\tau_1}(1-\alpha_w^{\tau_1}(T^{\tau_1} - T_0)) \\ & - k_{11}c_{p,w}\rho_w^{\tau_1}(T^{\tau_1} - T_0)\Bigg[\frac{1}{{\mu_w^2}^{\tau_1}}\frac{\partial \mu_w^{\tau_1}}{\partial T^{\tau_1}}(\frac{\partial {p_w}^{\tau_1}}{\partial {x_1}^{\tau_1}} + {\rho_w}^{\tau_1}g_1) \\ & + (\frac{2\rho_w^{\tau_1}}{\mu_w^{\tau_1}}g_1 + \frac{1}{\mu_w^{\tau_1}}\frac{\partial p_w^{\tau_1}}{\partial x_1^{\tau_1}})\alpha_w^{\tau_1}\Bigg]\rho_w^{\tau_1} - k_{12}c_{p,w}\rho_w^{\tau_1}(T^{\tau_1} - T_0) \\ & \cdot \Bigg[\frac{1}{{\mu_w^2}^{\tau_1}}\frac{\partial \mu_w^{\tau_1}}{\partial T^{\tau_1}}(\frac{\partial p_w^{\tau_1}}{\partial x_2^{\tau_1}} + \rho_w^{\tau_1}g_2) + (\frac{2\rho_w^{\tau_1}}{\mu_w^{\tau_1}}g_2 + \frac{1}{\mu_w^{\tau_1}}\frac{\partial p_w^{\tau_1}}{\partial x_2^{\tau_1}})\alpha_w^{\tau_1}\Bigg]\rho_w^{\tau_1} \end{aligned} \tag{A6}$$

$$
\begin{aligned}
K^{\tau_1}_{TT_{2,3}} &= \alpha_d(\lambda_s-\lambda_w)(b-\phi^{\tau_1})\frac{\partial T^{\tau_1}}{\partial x_2^{\tau_1}} - c_{p,w}\rho_w^{\tau_1} f_{w,2}^{\tau_1}(1-\alpha_w^{\tau_1}(T^{\tau_1}-T_0)) \\
&\quad - k_{21}c_{p,w}\rho_w^{\tau_1}(T^{\tau_1}-T_0)\left[\frac{1}{\mu_w^{2\,\tau_1}}\frac{\partial \mu_w^{\tau_1}}{\partial T^{\tau_1}}(\frac{\partial p_w^{\tau_1}}{\partial x_1^{\tau_1}}+\rho_w^{\tau_1}g_1)\right. \\
&\quad \left. + (\frac{2\rho_w^{\tau_1}}{\mu_w^{\tau_1}}g_1+\frac{1}{\mu_w^{\tau_1}}\frac{\partial p_w^{\tau_1}}{\partial x_1^{\tau_1}})\alpha_w^{\tau_1}\right]\rho_w^{\tau_1} - k_{22}c_{p,w}\rho_w^{\tau_1}(T^{\tau_1}-T_0) \\
&\quad \cdot\left[\frac{1}{\mu_w^{2\,\tau_1}}\frac{\partial \mu_w^{\tau_1}}{\partial T^{\tau_1}}(\frac{\partial p_w^{\tau_1}}{\partial x_2^{\tau_1}}+\rho_w^{\tau_1}g_2)+(\frac{2\rho_w^{\tau_1}}{\mu_w^{\tau_1}}g_2+\frac{1}{\mu_w^{\tau_1}}\frac{\partial p_w^{\tau_1}}{\partial x_2^{\tau_1}})\alpha_w^{\tau_1}\right]\rho_w^{\tau_1}
\end{aligned}
\tag{A7}
$$

$$
\begin{aligned}
K^{\tau_1}_{TT_{3,3}} &= c_{p,w}\left[-\rho_w^{\tau_1}(b-\phi^{\tau_1})(T^{\tau_1}-T_0)\alpha_d\frac{1}{\Delta t}+\rho_w^{\tau_1}(b-\phi^{\tau_1})(\frac{\dot{\Omega}^{\tau_1}}{\Omega^{\tau_1}}\right. \\
&\quad + \frac{\dot{p}_w^{\tau_1}}{K_s^{\tau_1}}-\alpha_d\dot{T}^{\tau_1})-\rho_w^{\tau_1}\alpha_w^{\tau_1}(b-\phi^{\tau_1})(T^{\tau_1}-T_0)(\frac{\dot{\Omega}^{\tau_1}}{\Omega^{\tau_1}}+\frac{\dot{p}_w^{\tau_1}}{K_s^{\tau_1}} \\
&\quad - \alpha_d\dot{T}^{\tau_1})+\rho_w^{\tau_1}\alpha_d(T^{\tau_1}-T_0)(\frac{\dot{\Omega}^{\tau_1}}{\Omega^{\tau_1}}+\frac{\dot{p}_w^{\tau_1}}{K_s^{\tau_1}}-\alpha_d\dot{T}^{\tau_1})-\rho_w^{\tau_1}\phi^{\tau_1} \\
&\quad \cdot(T^{\tau_1}-T_0)(\frac{\partial\alpha_w^{\tau_1}}{\partial T^{\tau_1}}\dot{T}^{\tau_1}+\alpha_w^{\tau_1}\frac{1}{\Delta t})+\rho_w^{\tau_1}\phi^{\tau_1}(\frac{\dot{P}_w^{\tau_1}}{\chi_w}-\alpha_w^{\tau_1}\dot{T}^{\tau_1}) \\
&\quad - \rho_w^{\tau_1}(b-\phi^{\tau_1})(T^{\tau_1}-T_0)\alpha_d(\frac{\dot{P}_w^{\tau_1}}{\chi_w}-\alpha_w^{\tau_1}\dot{T}^{\tau_1})-\rho_w^{\tau_1}\alpha_w\phi^{\tau_1}(T^{\tau_1} \\
&\quad - T_0)(\frac{\dot{P}_w^{\tau_1}}{\chi_w}-\alpha_w^{\tau_1}\dot{T}^{\tau_1})+\rho_w^{\tau_1}\phi^{\tau_1}\frac{1}{\Delta t}-\rho_w^{\tau_1}\alpha_w\phi^{\tau_1}\dot{T}^{\tau_1} \\
&\quad - \rho_w^{\tau_1}(b-\phi^{\tau_1})\alpha_d\dot{T}^{\tau_1}-\rho_w^{\tau_1}\alpha_w\phi^{\tau_1}(T^{\tau_1}-T_0)\frac{\dot{\Omega}^{\tau_1}}{\Omega^{\tau_1}}+\rho_w^{\tau_1}\phi^{\tau_1}\frac{\dot{\Omega}^{\tau_1}}{\Omega^{\tau_1}} \\
&\quad \left. - \rho_w^{\tau_1}(b-\phi^{\tau_1})\alpha_d(T^{\tau_1}-T_0)\frac{\dot{\Omega}^{\tau_1}}{\Omega^{\tau_1}}\right]+c_{p,s}\left[-\rho_s^{\tau_1}\frac{\phi^{\tau_1}}{1-\phi^{\tau_1}}(b\right. \\
&\quad - \phi^{\tau_1})\alpha_d\dot{T}^{\tau_1}+\rho_s(b-\phi^{\tau_1})\alpha_d(T^{\tau_1}-T_0)(\frac{b-1}{1-\phi^{\tau_1}}\frac{\dot{\Omega}^{\tau_1}}{\Omega^{\tau_1}} \\
&\quad \left. + \frac{b-\phi^{\tau_1}}{1-\phi^{\tau_1}}\frac{\dot{p}_w^{\tau_1}}{K_s^{\tau_1}}-\frac{b-\phi^{\tau_1}}{1-\phi^{\tau_1}}\alpha_d\dot{T}^{\tau_1})+\rho_s^{\tau_1}(1-\phi^{\tau_1})\frac{1}{\Delta t}\right]
\end{aligned}
\tag{A8}
$$

The stiffness matrices of the coupling between the flow and mechanical processes are:

$$
K^{\tau_1}_{MW(3\times4)} = \begin{bmatrix} K_{MW_{1,1}} & K_{MW_{1,2}} & K_{MW_{1,3}} & K_{MW_{1,4}} \\ K_{MW_{2,1}} & K_{MW_{2,2}} & K_{MW_{2,3}} & K_{MW_{2,4}} \\ A+\dot{M}_w^{\tau_1} & 0 & 0 & A+\dot{M}_w^{\tau_1} \end{bmatrix} \tag{A9}
$$

where

$$
K^{\tau_1}_{MW_{1,1}} = -k_{11}\frac{\rho_w^{\tau_1}}{\mu_w^{\tau_1}}\frac{\partial p_w^{\tau_1}}{\partial x_1^{\tau_1}} \tag{A10}
$$

$$K^{\tau_1}_{MW_{1,2}} = -k_{12}\frac{\rho^{\tau_1}_w}{\mu^{\tau_1}_w}\frac{\partial p^{\tau_1}_w}{\partial x^{\tau_1}_1} + f^{\tau_1}_{w,2} \tag{A11}$$

$$K^{\tau_1}_{MW_{1,3}} = -k_{11}\frac{\rho^{\tau_1}_w}{\mu^{\tau_1}_w}\frac{\partial p^{\tau_1}_w}{\partial x^{\tau_1}_2} \tag{A12}$$

$$K^{\tau_1}_{MW_{1,4}} = -k_{12}\frac{\rho^{\tau_1}_w}{\mu^{\tau_1}_w}\frac{\partial p^{\tau_1}_w}{\partial x^{\tau_1}_2} - f^{\tau_1}_{w,1} \tag{A13}$$

$$K^{\tau_1}_{MW_{2,1}} = -k_{21}\frac{\rho^{\tau_1}_w}{\mu^{\tau_1}_w}\frac{\partial p^{\tau_1}_w}{\partial x^{\tau_2}_1} - f^{\tau_1}_{w,2} \tag{A14}$$

$$K^{\tau_1}_{MW_{2,2}} = -k_{22}\frac{\rho^{\tau_1}_w}{\mu^{\tau_1}_w}\frac{\partial p^{\tau_1}_w}{\partial x^{\tau_1}_1} \tag{A15}$$

$$K^{\tau_1}_{MW_{2,3}} = -k_{21}\frac{\rho^{\tau_1}_w}{\mu^{\tau_1}_w}\frac{\partial p^{\tau_1}_w}{\partial x^{\tau_1}_2} + f^{\tau_1}_{w,1} \tag{A16}$$

$$K^{\tau_1}_{MW_{2,4}} = -k_{22}\frac{\rho^{\tau_1}_w}{\mu^{\tau_1}_w}\frac{\partial p^{\tau_1}_w}{\partial x^{\tau_1}_2} \tag{A17}$$

$$A = \rho^{\tau_1}_w\left[(\frac{\dot{p}^{\tau_1}_w}{\chi_w} - \alpha^{\tau_1}_w\dot{T}^{\tau_1} - \frac{\dot{p}^{\tau_1}_w}{K_s})(b-\phi^{\tau_1}) + b(\frac{1}{\Delta t} - \frac{\dot{\Omega}^{\tau_1}}{\Omega^{\tau_1}})\right] \tag{A18}$$

$$K^{\tau_1}_{WM(4\times3)} = \begin{bmatrix} 0 & 0 & -1 \\ 0 & 0 & 0 \\ 0 & 0 & 0 \\ 0 & 0 & -1 \end{bmatrix} \tag{A19}$$

The stiffness matrices of the coupling between the thermal and mechanical processes are:

$$K^{\tau_1}_{MT(3\times4)} = \begin{bmatrix} K_{MT_{1,1}} & K_{MT_{1,2}} & K_{MT_{1,3}} & K_{MT_{1,4}} \\ K_{MT_{2,1}} & K_{MT_{2,2}} & K_{MT_{2,3}} & K_{MT_{2,4}} \\ D + \dot{S}^{\tau_1}_T & 0 & 0 & D + \dot{S}^{\tau_1}_T \end{bmatrix} \tag{A20}$$

where

$$K^{\tau_1}_{MT_{1,1}} = -(\lambda_s - \lambda_w)(b-\phi^{\tau_1})\frac{\partial T^{\tau_1}}{\partial x^{\tau_1}_1} - c_{p,w}\rho^{\tau_1}_w(T^{\tau_1} - T_0)k_{11}\frac{\rho^{\tau_1}_w}{\mu^{\tau_1}_w}\frac{\partial p^{\tau_1}_w}{\partial x^{\tau_1}_1} \tag{A21}$$

$$K^{\tau_1}_{MT_{1,2}} = -c_{p,w}\rho^{\tau_1}_w(T^{\tau_1} - T_0)k_{12}\frac{\rho^{\tau_1}_w}{\mu^{\tau_1}_w}\frac{\partial p^{\tau_1}_w}{\partial x^{\tau_1}_1} + f^{\tau_1}_{T,2} \tag{A22}$$

$$K^{\tau_1}_{MT_{1,3}} = -c_{p,w}\rho^{\tau_1}_w(T^{\tau_1} - T_0)k_{11}\frac{\rho^{\tau_1}_w}{\mu^{\tau_1}_w}\frac{\partial p^{\tau_1}_w}{\partial x^{\tau_1}_2} \tag{A23}$$

$$K^{\tau_1}_{MT_{1,4}} = -(\lambda_s - \lambda_w)(b-\phi^{\tau_1})\frac{\partial T^{\tau_1}}{\partial x^{\tau_1}_1} - c_{p,w}\rho^{\tau_1}_w(T^{\tau 1} - T_0)k_{12}\frac{\rho^{\tau_1}_w}{\mu^{\tau_1}_w}\frac{\partial p^{\tau_1}_w}{\partial x^{\tau_1}_2} - f^{\tau_1}_{T,1} \tag{A24}$$

$$K^{\tau_1}_{MT_{2,1}} = -(\lambda_s - \lambda_w)(b-\phi^{\tau_1})\frac{\partial T^{\tau_1}}{\partial x^{\tau_1}_2} - c_{p,w}\rho^{\tau_1}_w(T^{\tau_1} - T_0)k_{21}\frac{\rho^{\tau_1}_w}{\mu^{\tau_1}_w}\frac{\partial p^{\tau_1}_w}{\partial x^{\tau_1}_1} - f^{\tau_1}_{T,2} \tag{A25}$$

$$K^{\tau_1}_{MT_{2,2}} = -c_{p,w}\rho^{\tau_1}_w(T^{\tau_1}-T_0)k_{22}\frac{\rho^{\tau_1}_w}{\mu^{\tau_1}_w}\frac{\partial p^{\tau_1}_w}{\partial x^{\tau_1}_1} \tag{A26}$$

$$K^{\tau_1}_{MT_{2,3}} = -c_{p,w}\rho^{\tau_1}_w(T^{\tau_1}-T_0)k_{21}\frac{\rho^{\tau_1}_w}{\mu^{\tau_1}_w}\frac{\partial p^{\tau_1}_w}{\partial x^{\tau_1}_2} + f^{\tau_1}_{T,1} \tag{A27}$$

$$K^{\tau_1}_{MT_{2,4}} = -(\lambda_s-\lambda_w)(b-\phi^{\tau_1})\frac{\partial T^{\tau_1}}{\partial x_2} - c_{p,w}\rho^{\tau_1}_w(T^{\tau_1}-T_0)k_{22}\frac{\rho^{\tau_1}_w}{\mu^{\tau_1}_w}\frac{\partial p^{\tau_1}_w}{\partial x^{\tau_1}_2} \tag{A28}$$

$$\begin{aligned} D = c_{p,w}\Bigg[& b\rho^{\tau_1}_w(T^{\tau_1}-T_0)(\frac{1}{\Delta t}-\frac{\dot{\Omega}^{\tau_1}}{\Omega^{\tau_1}}) - \rho^{\tau_1}_w(b-\phi^{\tau_1})(T^{\tau_1}-T_0)(\frac{\dot{\Omega}^{\tau_1}}{\Omega^{\tau_1}} \\ & + \frac{\dot{p}^{\tau_1}_w}{K^{\tau_1}_s} - \alpha_d\dot{T}^{\tau_1}) + \rho^{\tau_1}_w(b-\phi^{\tau_1})(T^{\tau_1}-T_0)(\frac{\dot{p}^{\tau_1}_w}{\chi_w} - \alpha^{\tau_1}_w\dot{T}^{\tau_1}) \\ & + \rho^{\tau_1}_w(b-\phi^{\tau_1})\dot{T}^{\tau_1} + \rho^{\tau_1}_w(b-\phi^{\tau_1})(T^{\tau_1}-T_0)\frac{\dot{\Omega}^{\tau_1}}{\Omega^{\tau_1}}\Bigg] \\ & - c_{p,s}\rho^{\tau_1}_s\left[\frac{1-b}{1-\phi^{\tau_1}} - (b-\phi^{\tau_1})\right]\dot{T}^{\tau_1} \end{aligned} \tag{A29}$$

$$K^{\tau_1}_{TM(4\times3)} = \begin{bmatrix} 0 & 0 & -\alpha^{\tau_1}_d(C_{1111}+C_{1122}) \\ 0 & 0 & -\alpha^{\tau_1}_d(C_{1211}+C_{1222}) \\ 0 & 0 & -\alpha^{\tau_1}_d(C_{2111}+C_{2122}) \\ 0 & 0 & -\alpha^{\tau_1}_d(C_{2211}+C_{2222}) \end{bmatrix} \tag{A30}$$

The stiffness matrices of the coupling between the flow and thermal processes are:

$$K^{\tau_1}_{WT(3\times3)} = \begin{bmatrix} K_{WT_{1,1}} & K_{WT_{1,2}} & K_{WT_{1,3}} \\ K_{WT_{2,1}} & K_{WT_{2,2}} & K_{WT_{2,3}} \\ 0 & 0 & K_{WT_{3,3}} \end{bmatrix} \tag{A31}$$

$$K^{\tau_1}_{WT_{1,1}} = c_{p,w}\rho^{\tau_1}_w(T^{\tau_1}-T_0)k_{11}\frac{\rho^{\tau_1}_w}{\mu^{\tau_1}_w} \tag{A32}$$

$$K^{\tau_1}_{WT_{1,2}} = c_{p,w}\rho^{\tau_1}_w(T^{\tau_1}-T_0)k_{12}\frac{\rho^{\tau_1}_w}{\mu^{\tau_1}_w} \tag{A33}$$

$$\begin{aligned} K^{\tau_1}_{WT_{1,3}} = & -(\lambda_s-\lambda_w)\frac{b-\phi^{\tau_1}}{K_s}\frac{\partial T^{\tau_1}}{\partial x^{\tau_1}_1} - c_{p,w}\frac{\rho^{\tau_1}_w}{\chi_w}f^{\tau_1}_{w,1}(T^{\tau_1}-T_0) \\ & + k_{11}c_{p,w}\rho^{\tau_1}_w(T^{\tau_1}-T_0)(\frac{2\rho^{\tau_1}_w}{\mu^{\tau_1}_w}g_1 + \frac{1}{\mu^{\tau_1}_w}\frac{\partial p^{\tau_1}_w}{\partial x^{\tau_1}_1})\frac{\rho^{\tau_1}_w}{\chi_w} \\ & + k_{12}c_{p,w}\rho^{\tau_1}_w(T^{\tau_1}-T_0)(\frac{2\rho^{\tau_1}_w}{\mu^{\tau_1}_w}g_2 + \frac{1}{\mu^{\tau_1}_w}\frac{\partial p^{\tau_1}_w}{\partial x^{\tau_1}_2})\frac{\rho^{\tau_1}_w}{\chi_w} \end{aligned} \tag{A34}$$

$$K^{\tau_1}_{WT_{2,1}} = c_{p,w}\rho^{\tau_1}_w(T^{\tau_1}-T_0)k_{21}\frac{\rho^{\tau_1}_w}{\mu^{\tau_1}_w} \tag{A35}$$

$$K^{\tau_1}_{WT_{2,2}} = c_{p,w}\rho^{\tau_1}_w(T^{\tau_1}-T_0)k_{22}\frac{\rho^{\tau_1}_w}{\mu^{\tau_1}_w} \tag{A36}$$

$$
\begin{aligned}
K^{\tau_1}_{WT_{2,3}} &= -(\lambda_s - \lambda_w)\frac{b-\phi^{\tau_1}}{K_s}\frac{\partial T^{\tau_1}}{\partial x_2^{\tau_1}} - c_{p,w}\frac{\rho_w^{\tau_1}}{\chi_w} f_{w,2}^{\tau_1}(T^{\tau_1} - T_0) \\
&\quad + k_{11} c_{p,w}\rho_w^{\tau_1}(T^{\tau_1} - T_0)\left(\frac{2\rho_w^{\tau_1}}{\mu_w^{\tau_1}} g_1 + \frac{1}{\mu_w^{\tau_1}}\frac{\partial p_w^{\tau_1}}{\partial x_1^{\tau_1}}\right)\frac{\rho_w^{\tau_1}}{\chi_w} \\
&\quad + k_{12} c_{p,w}\rho_w^{\tau_1}(T^{\tau_1} - T_0)\left(\frac{2\rho_w^{\tau_1}}{\mu_w^{\tau_1}} g_2 + \frac{1}{\mu_w^{\tau_1}}\frac{\partial p_w^{\tau_1}}{\partial x_2^{\tau_1}}\right)\frac{\rho_w^{\tau_1}}{\chi_w}
\end{aligned} \tag{A37}
$$

$$
\begin{aligned}
K^{\tau_1}_{WT_{3,3}} &= c_{p,w}\Bigg[\rho_w^{\tau_1}(b-\phi^{\tau_1})(T^{\tau_1} - T_0)\frac{1}{K_s \cdot \Delta t} + \rho_w^{\tau_1}(b-\phi^{\tau_1})(T^{\tau_1} \\
&\quad - T_0)\left(\frac{\dot{\Omega}^{\tau_1}}{\Omega^{\tau_1}} + \frac{\dot{p}_w^{\tau_1}}{K_s^{\tau_1}} - \alpha_d \dot{T}^{\tau_1}\right)\left(\frac{1}{\chi_w} - \frac{1}{K_s}\right) + \frac{\rho_w^{\tau_1}}{\chi_w \cdot \Delta t}\phi^{\tau_1}(T^{\tau_1} \\
&\quad - T_0) + \rho_w^{\tau_1}\frac{b-\phi^{\tau_1}}{K_s}\left(\frac{\dot{p}_w^{\tau_1}}{\chi_w} - \alpha_w^{\tau_1}\dot{T}^{\tau_1}\right)(T^{\tau_1} - T_0) + \frac{\rho_w^{\tau_1}}{\chi_w}\phi^{\tau_1}\left(\frac{\dot{p}_w^{\tau_1}}{\chi_w}\right. \\
&\quad \left. - \alpha_w^{\tau_1}\dot{T}^{\tau_1}\right)(T^{\tau_1} - T_0) + \frac{\rho_w^{\tau_1}}{\chi_w}\phi^{\tau_1}\dot{T}^{\tau_1} + \rho_w^{\tau_1}(b-\phi^{\tau_1})\frac{\dot{T}^{\tau_1}}{K_s} \\
&\quad + \frac{\rho_w^{\tau_1}}{\chi_w}\phi^{\tau_1}(T^{\tau_1} - T_0)\frac{\dot{\Omega}^{\tau_1}}{\Omega^{\tau_1}} + \rho_w^{\tau_1}\frac{b-\phi^{\tau_1}}{K_s}(T^{\tau_1} - T_0)\frac{\dot{\Omega}^{\tau_1}}{\Omega^{\tau_1}}\Bigg] \\
&\quad + c_{p,s}\left[\rho_s^{\tau_1}\frac{b-1}{K_s}(T^{\tau_1} - T_0)\frac{\dot{\Omega}^{\tau_1}}{\Omega^{\tau_1}} + \rho_s^{\tau_1}\frac{b-\phi^{\tau_1}}{K_s}\frac{\phi^{\tau_1}}{1-\phi^{\tau_1}}\dot{T}^{\tau_1}\right]
\end{aligned} \tag{A38}
$$

$$
K^{\tau_1}_{TW(3\times 3)} = \begin{bmatrix} 0 & 0 & K_{TW_{1,3}} \\ 0 & 0 & K_{TW_{2,3}} \\ 0 & 0 & K_{TW_{3,3}} \end{bmatrix} \tag{A39}
$$

$$
\begin{aligned}
K^{\tau_1}_{TW_{1,3}} &= -k_{11}\Bigg[\frac{1}{\mu_w^{2\,\tau_1}}\frac{\partial \mu_w^{\tau_1}}{\partial T^{\tau_1}}\left(\frac{\partial p_w^{\tau_1}}{\partial x_1^{\tau_1}} + \rho_w^{\tau_1} g_1\right) + \left(\frac{2\rho_w^{\tau_1}}{\mu_w^{\tau_1}} g_1 + \frac{1}{\mu_w^{\tau_1}}\frac{\partial p_w^{\tau_1}}{\partial x_1^{\tau_1}}\right) \\
&\quad \cdot \alpha_w^{\tau_1}\Bigg]\rho_w^{\tau_1} - k_{12}\Bigg[\frac{1}{\mu_w^{2\,\tau_1}}\frac{\partial \mu_w^{\tau_1}}{\partial T^{\tau_1}}\left(\frac{\partial p_w^{\tau_1}}{\partial x_2^{\tau_1}} + \rho_w^{\tau_1} g_2\right) + \left(\frac{2\rho_w^{\tau_1}}{\mu_w^{\tau_1}} g_2\right. \\
&\quad \left. + \frac{1}{\mu_w^{\tau_1}}\frac{\partial p_w^{\tau_1}}{\partial x_2^{\tau_1}}\right)\alpha_w^{\tau_1}\Bigg]\rho_w^{\tau_1}
\end{aligned} \tag{A40}
$$

$$
\begin{aligned}
K^{\tau_1}_{TW_{2,3}} &= -k_{21}\Bigg[\frac{1}{\mu_w^{2\,\tau_1}}\frac{\partial \mu_w^{\tau_1}}{\partial T^{\tau_1}}\left(\frac{\partial p_w^{\tau_1}}{\partial x_1^{\tau_1}} + \rho_w^{\tau_1} g_1\right) + \left(\frac{2\rho_w^{\tau_1}}{\mu_w^{\tau_1}} g_1 + \frac{1}{\mu_w^{\tau_1}}\frac{\partial p_w^{\tau_1}}{\partial x_1^{\tau_1}}\right) \\
&\quad \cdot \alpha_w^{\tau_1}\Bigg]\rho_w^{\tau_1} - k_{22}\Bigg[\frac{1}{\mu_w^{2\,\tau_1}}\frac{\partial \mu_w^{\tau_1}}{\partial T^{\tau_1}}\left(\frac{\partial p_w^{\tau_1}}{\partial x_2^{\tau_1}} + \rho_w^{\tau_1} g_2\right) + \left(\frac{2\rho_w^{\tau_1}}{\mu_w^{\tau_1}} g_2\right. \\
&\quad \left. + \frac{1}{\mu_w^{\tau_1}}\frac{\partial p_w^{\tau_1}}{\partial x_2^{\tau_1}}\right)\alpha_w^{\tau_1}\Bigg]\rho_w^{\tau_1}
\end{aligned} \tag{A41}
$$

$$
\begin{aligned}
K^{\tau_1}_{TW_{3,3}} &= -\rho_w^{\tau_1}\Bigg[\left(\frac{\dot{p}_w^{\tau_1}}{\chi_w} - \alpha_w^{\tau_1}\dot{T}^{\tau_1} - \frac{\dot{p}_w^{\tau_1}}{K_s}\right)[(b-\phi^{\tau_1})\alpha_d + \alpha_w^{\tau_1}\phi^{\tau_1}] \\
&\quad + \left(\frac{\alpha_w^{\tau_1}}{\Delta t} + \frac{\partial \alpha_w^{\tau_1}}{\partial T^{\tau_1}}\dot{T}^{\tau_1}\right)\phi^{\tau_1} + b\alpha_d\left(\frac{\dot{p}_w^{\tau_1}}{K_s} + \frac{\dot{\Omega}^{\tau_1}}{\Omega^{\tau_1}}\right)\Bigg]
\end{aligned} \tag{A42}
$$

$G3^{\tau_1}_{(2\times3)}$, same as $G1^{\tau_1}_{(2\times4)}$ and $G2^{\tau_1}_{(2\times3)}$, being the additional contribution of gravity volume force reads:

$$G1_{(2\times4)} = \begin{bmatrix} -b\rho_w^{\tau_1} g_1 & 0 & 0 & -b\rho_w^{\tau_1} g_1 \\ -b\rho_w^{\tau_1} g_2 & 0 & 0 & -b\rho_w^{\tau_1} g_2 \end{bmatrix} \tag{A43}$$

$$G2_{(2\times3)} = \begin{bmatrix} 0 & 0 & -\rho_w^{\tau_1}\left(\frac{b-\phi^{\tau_1}}{K_s} + \frac{\phi^{\tau_1}}{\chi_w}\right) g_1 \\ 0 & 0 & -\rho_w^{\tau_1}\left(\frac{b-\phi^{\tau_1}}{K_s} + \frac{\phi^{\tau_1}}{\chi_w}\right) g_2 \end{bmatrix} \tag{A44}$$

$$G3_{(2\times3)} = \begin{bmatrix} 0 & 0 & \rho_w^{\tau_1}\left[(b-\phi^{\tau_1})\alpha_d + \alpha_w^{\tau_1}\phi^{\tau_1}\right] g_1 \\ 0 & 0 & \rho_w^{\tau_1}\left[(b-\phi^{\tau_1})\alpha_d + \alpha_w^{\tau_1}\phi^{\tau_1}\right] g_2 \end{bmatrix} \tag{A45}$$

References

Abelev AV, Lade PV (2004) Characterization of failure in cross-anisotropic soils. Journal of Engineering Mechanics 130(5):599–606. https://doi.org/10.1061/(asce)0733-9399(2004)130:5(599)

Amadei B (2012) Rock anisotropy and the theory of stress measurements, vol 2. springer science & Business media

Armand G, Leveau F, Nussbaum C, et al. (2014) Geometry and properties of the excavation-induced fractures at the meuse/haute-marne url drifts. Rock mechanics and rock engineering 47(1):21–41. https://doi.org/10.1007/s00603-012-0339-6

Armand G, Bumbieler F, Conil N, et al. (2017) Main outcomes from in situ thermo-hydro-mechanical experiments programme to demonstrate feasibility of radioactive high-level waste disposal in the callovo-oxfordian claystone. Journal of Rock Mechanics and Geotechnical Engineering 9(3):415–427. https://doi.org/https://doi.org/10.1016/j.jrmge.2017.03.004

Barnichon JD (1998) Finite element modelling in structural and petroleum geology. PhD thesis, Universite de Liege

Bossart P, Meier PM, Moeri A, et al. (2002) Geological and hydraulic characterisation of the excavation disturbed zone in the opalinus clay of the mont terri rock laboratory. Engineering Geology 66(1-2):19–38. https://doi.org/10.1016/S0013-7952(01)00140-5

Bossart P, Trick T, Meier PM, et al. (2004) Structural and hydrogeological characterisation of the excavation-disturbed zone in the opalinus clay (mont terri project, switzerland). Applied clay science 26(1-4):429–448. https://doi.org/10.1016/j.clay.2003.12.018

Braun P (2019) Thermo-hydro-mechanical behavior of the callovo-oxfordian claystone: Effects of stress paths and temperature changes. PhD thesis, Université Paris-Est

Braun P, Delage P, Ghabezloo S, et al. (2022) Inducing tensile failure of claystone through thermal pressurization in a novel triaxial device. Rock Mechanics and Rock Engineering pp 1–19. https://doi.org/10.1007/s00603-022-02838-3

Bumbieler F, Plúa C, Tourchi S, et al. (2021) Feasibility of constructing a full-scale radioactive high-level waste disposal cell and characterization of its thermo-hydro-mechanical behavior. International Journal of Rock Mechanics and Mining Sciences 137:104,555. https://doi.org/10.1016/j.ijrmms.2020.104555

Chambon R, Moullet JC (2004) Uniqueness studies in boundary value problems involving some second gradient models. Computer methods in applied mechanics and engineering 193(27-29):2771–2796. https://doi.org/10.1016/j.cma.2003.10.017

Chambon R, Caillerie D, El Hassan N (1998) One-dimensional localisation studied with a second grade model. European Journal of Mechanics-A/Solids 17(4):637–656. https://doi.org/10.1016/S0997-7538(99)80026-6

Chambon R, Caillerie D, Matsuchima T (2001) Plastic continuum with microstructure, local second gradient theories for geomaterials: localization studies. International journal of solids and structures 38(46-47):8503–8527. https://doi.org/10.1016/S0020-7683(01)00057-9

Charlier R (1987) Approche unifiée de quelques problèmes non linéaires de mécanique des milieux continus par la méthode des éléments finis: Grandes déformations des métaux et des sols, contact unilatéral de solides, conduction thermique et écoulements en milieu poreux

Chen G, Dizier A, Li X, et al. (2021) Numerical prediction of the large-scale in situ praclay heater test in the boom clay. Rock Mechanics and Rock Engineering 54(5):2197–2218. https://doi.org/10.1007/s00603-021-02405-2

Chen L, Shao JF, Huang H (2010) Coupled elastoplastic damage modeling of anisotropic rocks. Computers and Geotechnics 37(1-2):187–194. https://doi.org/10.1016/j.compgeo.2009.09.001

Collin F, Li XL, Radu JP, et al. (2002) Thermo-hydro-mechanical coupling in clay barriers. Engineering Geology 64(2-3):179–193. https://doi.org/10.1016/S0013-7952(01)00124-7

Collin F, Chambon R, Charlier R (2006) A finite element method for poro mechanical modelling of geotechnical problems using local second gradient models. International journal for numerical methods in engineering 65(11):1749–1772. https://doi.org/10.1002/nme.1515

Collin F, Levasseur S, Chambon R (2009) Numerical post failure methods in multiphysical problems. European journal of environmental and civil engineering 13(7-8):983–1004. https://doi.org/10.3166/ejece.13.983-1004

Conil N, Vitel M, Plua C, et al. (2020) In situ investigation of the thm behavior of the callovo-oxfordian claystone. Rock Mechanics and Rock Engineering 53:2747–2769. https://doi.org/https://doi.org/10.1007/s00603-020-02073-8

Cosserat E, Cosserat F (1909) Theorie des corps deformables

Coussy O (2004) Poromechanics. John Wiley & Sons

Croisé J, Schlickenrieder L, Marschall P, et al. (2004) Hydrogeological investigations in a low permeability claystone formation: the mont terri rock laboratory. Physics and Chemistry of the Earth, Parts A/B/C 29(1):3–15. https://doi.org/10.1016/j.pce.2003.11.008

Cui YJ, Sultan N, Delage P (2000) A thermomechanical model for saturated clays. Canadian Geotechnical Journal 37(3):607–620. https://doi.org/10.1139/cgj-37-3-607

De Bruyn D, Labat S (2002) The second phase of atlas: the continuation of a running thm test in the hades underground research facility at mol. Engineering Geology 64(2-3):309–316. https://doi.org/https://doi.org/10.1016/S0013-7952(01)00109-0

Diederichs M (2003) Manuel rocha medal recipient rock fracture and collapse under low confinement conditions. Rock Mechanics and Rock Engineering 36(5):339–381. https://doi.org/10.1007/s00603-003-0015-y

Dirksen C (1970) Effects of temperature and heat on engineering behavior of soils: Highway research board, special report 103. proceedings of an international conference held at washington, dc, jan. 16, 1969, with support of the national science foundation. available from highway research board, national academy of sciences, 2101 constitution ave., washington, dc 20418. 8.00papercover— 10.00 hard cover, 300 p.

Dizier A, Chen G, Verstricht J, et al. (2021) The large-scale in situ praclay heater test: First observations on the in situ thermo-hydro-mechanical behaviour of boom clay. International Journal of Rock Mechanics and Mining Sciences 137:104,558. https://doi.org/10.1016/j.ijrmms.2020.104558

Eurad Hitec R (2019) EURAD WP HITEC Milestone report 49 – Selection of benchmark exercises for task 2.3. Tech. rep.

Félix B, Lebon P, Miguez R, et al. (1996) A review of the andra's research programmes on the thermo-hydromechanical behavior of clay in connection

with the radioactive waste disposal project in deep geological formations. Engineering geology 41(1-4):35–50. https://doi.org/10.1016/0013-7952(95)00025-9

Garitte B, Nguyen T, Barnichon J, et al. (2017) Modelling the mont terri hed experiment for the thermal–hydraulic–mechanical response of a bedded argillaceous formation to heating. Environmental Earth Sciences 76:1–20. https://doi.org/https://doi.org/10.1007/s12665-017-6662-1

Gens A, Vaunat J, Garitte B, et al. (2011) In situ behaviour of a stiff layered clay subject to thermal loading: observations and interpretation. In: Stiff Sedimentary Clays: Genesis and Engineering Behaviour: Géotechnique Symposium in Print 2007, Thomas Telford Ltd, pp 123–144, https://doi.org/10.1680/ssc.41080.0011

Germain P (1973) The method of virtual power in continuum mechanics. part 2: Microstructure. SIAM Journal on Applied Mathematics 25(3):556–575

Ghabezloo S, Sulem J (2010) Temperature induced pore fluid pressurization in geomaterials. arXiv preprint arXiv:10116501 https://doi.org/10.48550/arXiv.1011.6501

Ghabezloo S, Sulem J, Saint-Marc J (2009) The effect of undrained heating on a fluid-saturated hardened cement paste. Cement and Concrete Research 39(1):54–64. https://doi.org/10.1016/j.cemconres.2008.09.004

Hoek E, Brown ET (1980) Empirical strength criterion for rock masses. Journal of the geotechnical engineering division 106(9):1013–1035. https://doi.org/10.1061/AJGEB6.0001029

Hueckel T, Borsetto M (1990) Thermoplasticity of saturated soils and shales: constitutive equations. Journal of geotechnical engineering 116(12):1765–1777. https://doi.org/10.1061/(ASCE)0733-9410(1990)116:12(1765)

Jaeger J (1960) Shear failure of anistropic rocks. Geological magazine 97(1):65–72. https://doi.org/10.1017/S0016756800061100

Jobmann M, Polster M (2007) The response of opalinus clay due to heating: A combined analysis of in situ measurements, laboratory investigations and numerical calculations. Physics and Chemistry of the Earth, Parts A/B/C 32(8-14):929–936. https://doi.org/https://doi.org/10.1016/j.pce.2006.03.014

Kell GS (1975) Density, thermal expansivity, and compressibility of liquid water from 0. deg. to 150. deg.. correlations and tables for atmospheric pressure and saturation reviewed and expressed on 1968 temperature scale. Journal of Chemical and Engineering data 20(1):97–105. https://doi.org/

10.1021/je60064a005

Ken-Ichi K (1984) Distribution of directional data and fabric tensors. International journal of engineering science 22(2):149–164. https://doi.org/10.1016/0020-7225(84)90090-9

Lade PV (2007) Modeling failure in cross-anisotropic frictional materials. International Journal of Solids and Structures 44(16):5146–5162. https://doi.org/10.1016/j.ijsolstr.2006.12.027

Laloui L (2001) Thermo-mechanical behaviour of soils. Revue française de génie civil 5(6):809–843. https://doi.org/10.1080/12795119.2001.9692328

Laloui L, Cekerevac C (2003) Thermo-plasticity of clays: an isotropic yield mechanism. Computers and Geotechnics 30(8):649–660. https://doi.org/10.1016/j.compgeo.2003.09.001

Mindlin RD (1965) Second gradient of strain and surface-tension in linear elasticity. International Journal of Solids and Structures 1(4):417–438. https://doi.org/10.1016/0020-7683(65)90006-5

Modaressi H, Laloui L (1997) A thermo-viscoplastic constitutive model for clays. International journal for numerical and analytical methods in geomechanics 21(5):313–335. https://doi.org/10.1002/(sici)1096-9853(199705)21:5⟨313::aid-nag872⟩3.0.co;2-5

Monfared M, Sulem J, Delage P, et al. (2012) On the thm behaviour of a sheared boom clay sample: Application to the behaviour and sealing properties of the edz. Engineering Geology 124:47–58. https://doi.org/10.1016/j.enggeo.2011.10.002

Narkuniene A, Poskas G, Justinavicius D, et al. (2022) Thm response in the near field of an hlw disposal tunnel in the callovo-oxfordian clay host rock caused by the imposed heat flux at different water drainage conditions. Minerals 12(10):1187. https://doi.org/https://doi.org/10.3390/min12101187

Neerdael B, Boyazis J (1997) The belgium underground research facility: Status on the demonstration issues for radioactive waste disposal in clay. Nuclear Engineering and Design 176(1-2):89–96. https://doi.org/10.1016/s0029-5493(96)01346-5

Pardoen B, Collin F (2017) Modelling the influence of strain localisation and viscosity on the behaviour of underground drifts drilled in claystone. Computers and Geotechnics 85:351–367. https://doi.org/10.1016/j.compgeo.2016.05.017

Pardoen B, Levasseur S, Collin F (2015a) Using local second gradient model and shear strain localisation to model the excavation damaged zone in unsaturated claystone. Rock Mechanics and Rock Engineering 48(2):691–714. https://doi.org/10.1007/s00603-014-0580-2

Pardoen B, Seyedi D, Collin F (2015b) Shear banding modelling in cross-anisotropic rocks. International Journal of Solids and Structures 72:63–87. https://doi.org/10.1016/j.ijsolstr.2015.07.012

Pardoen B, Talandier J, Collin F (2016) Permeability evolution and water transfer in the excavation damaged zone of a ventilated gallery. International Journal of Rock Mechanics and Mining Sciences 85:192–208. https://doi.org/10.1016/j.ijrmms.2016.03.007

Peerlings Rd, Borst Rd, Brekelmans Wd, et al. (1996) Some observations on localization in non-local and gradient damage models. European Journal of Mechanics A, Solids 15(6):937–953

Pietruszczak S (2010) Fundamentals of plasticity in geomechanics. Crc Press Boca Raton, FL

Pietruszczak S, Mroz Z (1981) Finite element analysis of deformation of strain-softening materials. International Journal for Numerical Methods in Engineering 17(3):327–334. https://doi.org/10.1002/nme.1620170303

Pietruszczak S, Mroz Z (2000) Formulation of anisotropic failure criteria incorporating a microstructure tensor. Computers and Geotechnics 26(2):105–112. https://doi.org/10.1016/S0266-352X(99)00034-8

Pietruszczak S, Mroz Z (2001) On failure criteria for anisotropic cohesive-frictional materials. International journal for numerical and analytical methods in geomechanics 25(5):509–524. https://doi.org/10.1002/nag.141

Pietruszczak S, Lydzba D, Shao JF (2002) Modelling of inherent anisotropy in sedimentary rocks. International Journal of Solids and Structures 39(3):637–648. https://doi.org/10.1016/S0020-7683(01)00110-X

Pijaudier-Cabot G, Bažant ZP (1987) Nonlocal damage theory. Journal of engineering mechanics 113(10):1512–1533. https://doi.org/10.1061/(ASCE)0733-9399(1987)113:10(1512)

Plúa C, Vu MN, Seyedi DM, et al. (2021) Effects of inherent spatial variability of rock properties on the thermo-hydro-mechanical responses of a high-level radioactive waste repository. International Journal of Rock Mechanics and Mining Sciences 145:104,682. https://doi.org/https://doi.org/10.1016/j.ijrmms.2021.104682

Rattez H, Stefanou I, Sulem J, et al. (2018) Numerical analysis of strain localization in rocks with thermo-hydro-mechanical couplings using cosserat continuum. Rock Mechanics and Rock Engineering 51(10):3295–3311. https://doi.org/10.1007/s00603-018-1529-7

Romero E, Villar M, Lloret A (2005) Thermo-hydro-mechanical behaviour of two heavily overconsolidated clays. Engineering Geology 81(3):255–268. https://doi.org/10.1016/j.enggeo.2005.06.011

Rumble J (2019) Crc handbook of chemistry and physics (100th ed.). boca rotan, fl

Seyedi D, Plúa C, Vitel M, et al. (2021) Upscaling thm modeling from small-scale to full-scale in-situ experiments in the callovo-oxfordian claystone. International Journal of Rock Mechanics and Mining Sciences 144:104,582. https://doi.org/https://doi.org/10.1016/j.ijrmms.2020.104582

Shahrokhabadi S, Cao TD, Vahedifard F (2020) Thermo-hydro-mechanical modeling of unsaturated soils using isogeometric analysis: Model development and application to strain localization simulation. International Journal for Numerical and Analytical Methods in Geomechanics 44(2):261–292. https://doi.org/10.1002/nag.3015

Sun W (2015) A stabilized finite element formulation for monolithic thermo-hydro-mechanical simulations at finite strain. International Journal for Numerical Methods in Engineering 103(11):798–839. https://doi.org/10.1002/nme.4910

Tourchi S, Vaunat J, Gens A, et al. (2021) A full-scale in situ heating test in callovo-oxfordian claystone: observations, analysis and interpretation. Computers and Geotechnics 133:104,045. https://doi.org/10.1016/j.compgeo.2021.104045

Tsang CF, Bernier F, Davies C (2005) Geohydromechanical processes in the excavation damaged zone in crystalline rock, rock salt, and indurated and plastic clays—in the context of radioactive waste disposal. International Journal of Rock Mechanics and Mining Sciences 42(1):109–125. https://doi.org/10.1016/j.ijrmms.2004.08.003

Van Eekelen H (1980) Isotropic yield surfaces in three dimensions for use in soil mechanics. International Journal for Numerical and Analytical Methods in Geomechanics 4(1):89–101. https://doi.org/10.1002/nag.1610040107

Wileveau Y, Su K, Ghoreychi M (2007) A heating experiment in the argillites in the meuse/haute-marne underground research laboratory. In: International Conference on Radioactive Waste Management and Environmental Remediation, pp 939–944

Wu S, Wang X (2010) Mesh dependence and nonlocal regularization of one-dimensional strain softening plasticity. Journal of engineering mechanics 136(11):1354–1365. https://doi.org/10.1061/(asce)em.1943-7889.0000184

Yu Z, Shao JF, Vu MN, et al. (2021) Numerical study of thermo-hydro-mechanical responses of in situ heating test with phase-field model. International Journal of Rock Mechanics and Mining Sciences 138:104,542. https://doi.org/https://doi.org/10.1016/j.ijrmms.2020.104542

Zervos A, Papanastasiou P, Vardoulakis I (2001a) A finite element displacement formulation for gradient elastoplasticity. International Journal for Numerical Methods in Engineering 50(6):1369–1388. https://doi.org/10.1002/1097-0207(20010228)50:6⟨1369::AID-NME72⟩3.0.CO;2-K

Zervos A, Papanastasiou P, Vardoulakis I (2001b) Modelling of localisation and scale effect in thick-walled cylinders with gradient elastoplasticity. International Journal of Solids and Structures 38(30-31):5081–5095. https://doi.org/10.1016/S0020-7683(00)00337-1